Earth's Future

RESEARCH ARTICLE
10.1029/2025EF006112

Drivers of Future Indian Ocean Warming and Its Spatial Pattern in CMIP Models

S. Gopika[1,2], **K. Sadhvi**[3], **J. Vialard**[4], **V. Danielli**[5], **S. Neetu**[1], **and M. Lengaigne**[5]

[1]CSIR- National Institute of Oceanography, Goa, India, [2]School of Earth, Ocean and Atmospheric Sciences, Goa University, Goa, India, [3]Digital University Kerala (DUK), Trivandrum, India, [4]LOCEAN/IPSL, Sorbonne Universités (UPMC, Université Paris 06)-CNRS-IRD-MNHN, Paris, France, [5]MARBEC, IFREMER, IRD, University of Montpellier, Montpellier, France

Key Points:

- Average Tropical Indian Ocean warming is driven by reduced evaporative cooling due to weaker winds and higher near-surface humidity
- Warming pattern diversity stems from variations in the weakening zonal equatorial gradient and strengthening interhemispheric gradient
- Ocean dynamics control zonal equatorial gradient changes; while differential evaporative cooling affects interhemispheric gradient changes

Supporting Information:

Supporting Information may be found in the online version of this article.

Correspondence to:

M. Lengaigne,
matthieu.lengaigne@ird.fr

Citation:

Gopika, S., Sadhvi, K., Vialard, J., Danielli, V., Neetu, S., & Lengaigne, M. (2025). Drivers of future Indian Ocean warming and its spatial pattern in CMIP models. *Earth's Future*, *13*, e2025EF006112. https://doi.org/10.1029/2025EF006112

Received 2 OCT 2024
Accepted 27 MAR 2025

Author Contributions:

Conceptualization: J. Vialard, M. Lengaigne
Data curation: S. Gopika, K. Sadhvi, V. Danielli
Formal analysis: S. Gopika
Funding acquisition: J. Vialard, M. Lengaigne
Investigation: S. Gopika
Supervision: J. Vialard, S. Neetu, M. Lengaigne
Visualization: S. Gopika
Writing – original draft: S. Gopika, J. Vialard, M. Lengaigne

Abstract Coupled Model Intercomparison Project phases 5 and 6 (CMIP5/6) projections display substantial inter-model diversity in the future tropical Indian Ocean warming magnitude and spatial pattern. Here, we investigate the underlying physical mechanisms in 46 CMIP5/6 models using an upper-ocean heat budget framework that separates surface net air-sea flux changes into forcing and feedback components. The multi-model mean (MMM) basin-averaged warming is primarily driven by reduced evaporative cooling due to weaker surface winds related to reduction of both summer and winter monsoonal circulations and increased near-surface relative humidity, with inter-model variations in these parameters controlling warming diversity. The MMM warming pattern features a weakening equatorial gradient, resembling a positive Indian Ocean Dipole phase, and a strengthening interhemispheric gradient, both of which also dominate inter-model spread. Ocean dynamics modulate the amplitude of the MMM IOD-like pattern and its inter-model variability through the Bjerknes feedback, which couples the zonal equatorial SST gradient, equatorial winds, and thermocline slope. Interactions with the tropical Pacific may further contribute to this response. Meanwhile, stronger climatological winds enhance evaporative cooling in the Southern Hemisphere, reducing warming there, and strengthening the MMM interhemispheric SST gradient. The diversity in this interhemispheric gradient is linked to variations in cross-equatorial wind changes and their impact on latent heat flux forcing. This interhemispheric gradient strengthening is part of a broader pan-tropical pattern, with similar features in the Pacific and Atlantic Oceans. These findings clarify the relative roles of thermodynamic processes and ocean dynamics in shaping future tropical Indian Ocean warming.

Plain Language Summary The Tropical Indian Ocean is expected to warm further in the future, but the amount and pattern of warming vary widely across climate models. These differences matter because they shape regional weather, climate, and marine ecosystems in different ways. This study examines what drives Tropical Indian Ocean warming and why model projections differ. We find that weakening surface winds and higher near-surface humidity reduce evaporative cooling, allowing more heat to build up and driving overall warming. The warming pattern has two key features: (a) a decreasing temperature difference between the warmer eastern and cooler western equatorial Indian Ocean and (b) an increasing temperature difference between the warmer Northern and cooler Southern Indian Ocean. The east-west pattern is shaped by ocean-atmosphere interactions that control how heat moves within the ocean, with possible influences from changes in the Pacific Ocean. The north-south contrast, also observed in the Pacific and Atlantic, occurs because stronger winds in the Southern Hemisphere increase evaporation, limiting warming there and enhancing the temperature contrast with the Northern Hemisphere. These findings improve our understanding of regional climate change and help refine future climate projections.

1. Introduction

The Tropical Indian Ocean (TIO) has been steadily warming since the 1950s, primarily driven by anthropogenic forcing (Masson-Delmotte et al., 2021). Climate models from the Coupled Model Intercomparison Project (CMIP) project a basin-wide warming of nearly 3°C by the end of the 21st century under high-emission scenarios (Figure 1; Gopika et al., 2020). This warming has profound regional and global consequences. Regionally, it affects atmospheric circulation (Sharma et al., 2023), monsoonal rainfall (Sandeep & Ajayamohan, 2014), natural climate variability (Cai et al., 2014), tropical cyclones (Bell et al., 2020), and ocean productivity (Roxy et al., 2016). Globally, it may strengthen the Atlantic overturning circulation (Hu & Fedorov, 2019) and increase

Writing – review & editing: K. Sadhvi, S. Neetu

droughts occurrence in the Sahel (Beal et al., 2020). Given these far-reaching impacts, understanding the mechanisms driving the TIO warming is essential for improving climate predictions and guiding adaptation strategies.

Previous studies have identified two primary mechanisms driving the average TIO warming (Dong & Zhou, 2014; Dong et al., 2014; Du & Xie, 2008; Zhang & Li, 2014). First, increased downward longwave radiation, amplified by the water vapor feedback, plays a key role: a warmer atmosphere holds more water vapor, which is a greenhouse gas that amplifies the warming. Second, reduced evaporative cooling due to basin-wide surface wind reduction further amplifies this warming. These warming mechanisms are partially offset by a negative feedback. In which, increased evaporation due to warmer sea surface temperatures (SSTs) damps the warming through increased latent heat uptake. However, the relative importance of these drivers varies across studies, reflecting differences in methods and data sets.

The TIO warming is not spatially uniform, and this uneven warming pattern influences regional rainfall and atmospheric circulation. Regions that warm more than the tropical average experience reduced stability and increased rainfall, a phenomenon known as the "warmer-get-wetter" paradigm (Xie, 2020; Xie et al., 2010). This, in turn, affects atmospheric and oceanic circulation patterns, as well as the distribution of tropical cyclones. Relative Sea Surface Temperature (RSST), defined as local SST minus its tropical average, is a useful metric for assessing atmospheric stability changes (e.g., Izumo et al., 2020; Johnson & Xie, 2010). CMIP models project an enhanced warming in the western equatorial TIO and Arabian Sea, with comparatively weaker warming in the eastern equatorial TIO (Figures 1a and 1b; Cai et al., 2014; Sharma et al., 2023). This pattern, resembling the positive phase of the Indian Ocean Dipole (IOD; e.g. Saji et al., 1999), is often referred to as "IOD-like" (e.g., Zheng et al., 2013). It is characterized by a reduced equatorial SST gradient and a weakening of the TIO zonal atmospheric circulation (e.g., Held & Soden, 2006). Alongside this zonal asymmetry, warming is generally stronger in the northern TIO (Figures 1a and 1b), intensifying the interhemispheric SST gradient. This enhanced gradient shifts the Intertropical Convergence Zone northward (Byrne et al., 2018) and increases summer monsoonal rainfall (B. Wang et al., 2020).

The warming pattern in the tropical Indian Ocean results from a complex interplay of flux adjustments and ocean dynamics (Liu et al., 2015; Xie et al., 2010). A key process is the positive Bjerknes feedback (Bjerknes, 1969), whereby ocean dynamics amplify an IOD-like pattern by reducing the equatorial rainfall gradient, inducing easterly winds, and steepening the thermocline slope (e.g., Liu et al., 2015; Zhang & Li, 2014). Yet, the mechanisms that initiate this pattern remain debated. One hypothesis suggests that mean tropical warming weakens the Walker circulation, thereby generating equatorial easterly anomalies that trigger the IOD-like pattern via ocean dynamics (Ma et al., 2012; Sharma et al., 2023). Another proposes that the ocean dynamical thermostat mechanism (Clement et al., 1996) brings cooler subsurface waters to the surface in the eastern equatorial Indian Ocean during fall, limiting regional warming (Liu et al., 2015; Xie et al., 2010). Additionally, a stronger negative evaporative feedback over the warmer eastern region compared to the cooler west has also been advanced as a trigger (e.g., Liu et al., 2015; Zhang & Li, 2014). Overall, consensus on the relative roles of these mechanisms remains elusive.

Even less is understood about the mechanisms driving TIO interhemispheric SST gradient changes. Some studies attribute these changes to latent heat forcing, because the stronger southern hemisphere winds lead to more evaporative cooling, an effect possibly reinforced by the wind-evaporation-SST feedback (Xie et al., 2010). Others highlight the role of low-cloud cover and associated shortwave radiation changes, particularly in the southern TIO (Sharma et al., 2023).

Previous studies of the TIO warming mechanisms have typically focused on either individual models (e.g., Dong et al., 2014; Liu et al., 2015; Sharma et al., 2023; Xie et al., 2010) or the Multi-Model Mean (hereafter, MMM) response (e.g., Du & Xie, 2008; Zhang & Li, 2014). However, there is substantial inter-model diversity in CMIP projections. Under high-emission scenarios, 2100 basin-averaged warming ranges from +1.7°C to +4.2°C (Figure 1b). Similarly, projections for changes in equatorial zonal SST gradient (ZGRAD) range between 0°C and −1°C, while interhemispheric SST gradient (MGRAD) changes range from 0°C to +0.5°C (Figure 1b). Understanding the drivers behind these SST pattern variations is crucial for narrowing uncertainties in projected rainfall (Long et al., 2016; Ma & Xie, 2013). Although studies have examined the causes of inter-model diversity in SST patterns over regions such as the tropical Pacific (Ying & Huang, 2016a, 2016b), tropical Atlantic (Long & Xie, 2015) and Arctic (Yim et al., 2017), similar analyses for the TIO remain limited.

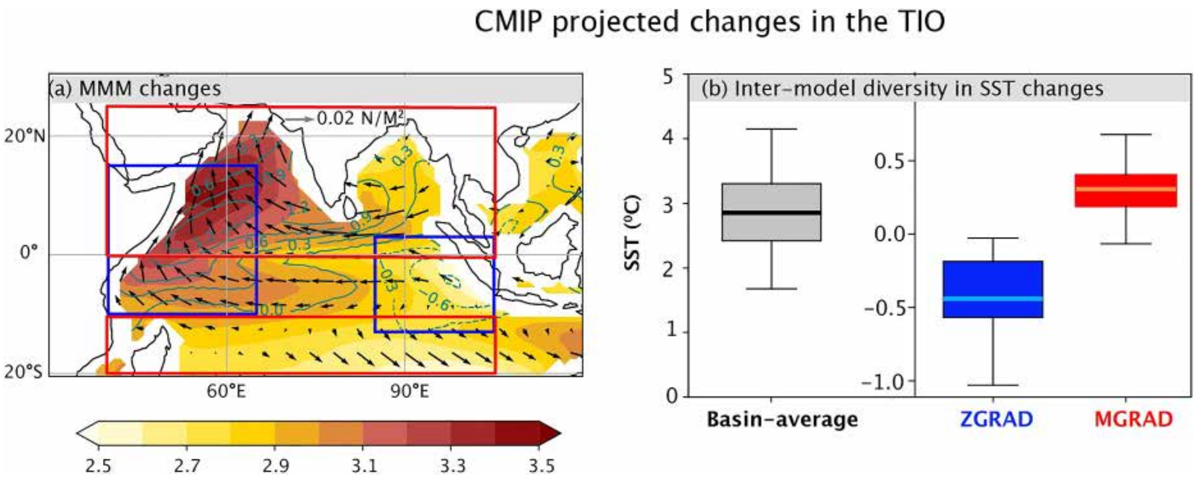

Figure 1. CMIP5/6 projected changes in the Tropical Indian Ocean (TIO). (a) Multi-Model Mean (MMM) projected changes for Sea Surface Temperature (SST, °C, shaded), precipitation (mm·day^{-1}, contours) and wind stress (N·m^{-2}, vectors). (b) Distribution of the projected changes in basin-averaged SST, zonal equatorial SST gradient (ZGRAD) and meridional inter-hemispheric SST gradient (MGRAD) across models. Horizontal lines indicate the MMM, the box edges indicate the lower and upper quartiles, and whiskers are the 10th and 90th percentiles. ZGRAD is calculated as SST changes averaged over the eastern TIO (85°–105°E; 13°S–3°N) minus those over the western TIO (40°–65°E, 10°S–15°N), displayed as blue boxes on panel (a). MGRAD is calculated as SST anomalies averaged over the northern TIO (30°−120°E; 0°–25°N) minus those averaged over the southern IO (30°−120°E; 20°–10°S), displayed as red boxes on panel (a).

Here, we investigate both the MMM and CMIP5 and CMIP6 inter-model diversity. Beyond exploring the drivers of the IOD-like warming pattern and its variability across models, we provide detailed analyses of an underexplored yet prominent TIO warming pattern: the strengthening of the interhemispheric SST gradient. Central to our approach is a heat budget framework inspired by Zhang and Li (2014, hereafter ZL14), which decomposes surface net air-sea flux changes into feedback (SST-dependent) and forcing (SST-independent) components, allowing a clear distinction between their respective influence. We further advance this framework by explicitly separating downward longwave flux into forcing and feedback components, addressing a limitation in ZL14, which excluded feedback contributions from downward longwave flux. Recent research (Pendergrass et al., 2018; Shakespeare & Roderick, 2022; Vargas Zeppetello et al., 2019) demonstrates that most of the downward longwave warming arises from feedback processes. Incorporating this component challenges previous findings that overemphasized the role of downward longwave forcing (Dong et al., 2014; ZL14). Additionally, this work extends the ZL14 methodology by deriving equations for both SST changes and RSST changes, enabling a detailed analysis of spatial variations in TIO warming. These methodological advancements collectively provide novel insights into the magnitude and spatial structure of TIO warming and its inter-model diversity.

This paper is organized as follows. Section 2 describes the data sets and processing methods. Section 3 reviews the ZL14 method, extends it to incorporate downwelling longwave flux feedback, and derives equations for the basin-average SST and RSST changes. Section 4 investigates the mechanisms behind the TIO basin-average warming, while Section 5 explores the factors shaping the TIO warming spatial pattern. Section 6 summarizes the findings and discusses their implications in the context of previous studies.

2. Data Sets and Processing

We analyze outputs from 46 CMIP simulations (Table 1), comprising 18 models from CMIP5 (Taylor et al., 2012) and 28 models from CMIP6 (Eyring et al., 2016). The model selection was based on the availability of key variables at a monthly frequency, including SST, surface heat flux components, near-surface wind speed, surface air temperature and humidity, cloud fraction, wind stress, precipitation, and sea surface height. Future projections were analyzed using unmitigated emission scenarios with an 8.5 Wm^{-2} radiative forcing: the RCP8.5 scenario for CMIP5 and SSP585 for CMIP6. For models with multiple ensemble members, only the first ensemble member was used.

All simulations were interpolated to a 1° × 1° grid over the TIO region (30°−120°E, 20°S–30°N). Because some models were already on standardized grids, they exhibited discontinuities in latent and sensible heat fluxes near coastlines. To address this, an ad-hoc coastal mask was applied to all variables and models, resulting in the

Table 1
CMIP5 and 6 Models Used in This Study

CMIP5 models	CMIP6 models
CSIRO–BOM.ACCESS1-0	CSIRO-ARCCSS.ACCESS-CM2
CSIRO–BOM.ACCESS1-3	CSIRO. ACCESS-ESM1-5
BCC.bcc-csm1-1	CCCma.CanESM5
BCC.bcc-csm1-1-m	CAS.CAS-ESM2-0
CCCma.CanESM2	NCAR.CESM2-WACCM
CNRM–CERFACS.CNRM-CM5	NCAR.CESM2
CSIRO–QCCCE.CSIRO-Mk3-6-0	CMCC.CMCC-CM2-SR5
NOAA-GFDL.GFDL-CM3	CMCC.CMCC-ESM2
NOAA-GFDL.GFDL-ESM2G	CNRM-CERFAcS.CNRM-CM6-1
NOAA-GFDL.GFDL-ESM2M	CNRM-CERFAcS.CNRM-ESM2-1
INM.inm-cm4	EC-Earth-Consortium.E3SM.E3SM1-1
IPSL.IPSL-CM5A-LR	EC-Earth-Consortium.EC-Earth3
IPSL.IPSL-CM5A-MR	EC-Earth-Consortium.EC-Earth3-CC
IPSL.IPSL-CM5B-LR	EC-Earth-Consortium.EC-Earth3-Veg
MIROC.MIROC-ESM	EC-Earth-Consortium.EC-Earth3-Veg-LR
MIROC.MIROC-ESM-CHEM	CAS.FGOALS-g3
MIROC.MIROC5	NOAA-GFDL.GFDL-CM4
MRI.MRI-CGCM3	NOAA-GFDL.GFDL-ESM4
	IPSL.IPSL-CM6A-LR
	MIROC.MIROC-ES2L
	MIROC.MIROC6
	MPI-M.MPI-ESM1-2-HR
	MPI-M.MPI-ESM1-2-LR
	MRI.MRI-ESM2-0
	NCC.NorESM2-LM
	NCC.NorESM2-MM
	AS-RCEC.TaiESM1
	MOHC.UKESM1-0-LL

Note. List of the 46 models (18 CMIP5 and 28 CMIP6) used in this study, with the institution name indicated first, followed by a dot and the model name.

exclusion of some coastal data points. The “present-day” period is defined as the 1958–1977 average, while the “future” period is defined as the 2068–2087 average. Future changes are denoted as Δ, representing the future minus present-day averages. These periods were chosen to align with a related study using an Ocean General Circulation Model (Lengaigne et al., 2025), though our results remain consistent when considering more commonly used periods (e.g., 1900–1920 and 2080–2099). The MMM is the average across the 46 available CMIP5 and CMIP6 simulations.

Surface fluxes are considered positive when downward (i.e., when they contribute to ocean warming). Quantities averaged over the TIO (30°E−120°E, 20°S–30°N) are denoted with an overbar, while deviations from these average TIO quantities are noted with a prime and referred to as “relative.” RSST is used as a proxy for atmospheric vertical stability and to highlight changes in the SST spatial pattern (e.g., Xie et al., 2010). While RSST is conventionally defined as the local SST minus the tropical mean (20°N–20°S), subtracting the TIO (30°E−120°E, 20°S–30°N) mean yields nearly identical results.

3. Simple Equation for the SST Change

This section presents the simple heat budget framework for diagnosing the mechanisms driving future SST and RSST changes. Section 3.1 reviews the original formulation by ZL14, while Section 3.2 details our refinements, primarily incorporating a downward longwave flux feedback. Section 3.3 derives equations for basin-averaged SST ($\overline{\Delta T}$) and RSST ($\Delta T'$) changes and explains the decomposition of the inter-model variances in these two quantities.

3.1. ZL14 Original Equation

ZL14 employed a surface budget approach based on Xie et al. (2010) to derive their diagnostic equation for projected SST changes ΔT, allowing the identification of key processes controlling SST change. This approach assumes a balance between changes in net surface flux (ΔQ) and oceanic fluxes into the mixed layer (hereafter referred to as ocean processes, ΔO), which includes lateral and vertical advection, lateral and vertical mixing, and entrainment. ΔO is expressed as equivalent heat fluxes (in $\text{W}\cdot\text{m}^{-2}$) and diagnosed as $\Delta O = -\Delta Q$. ΔQ is further decomposed into two components: $\Delta Q_{\text{For}} - \alpha\Delta T$, where $\alpha\Delta T$ represents the *feedback* component, which explicitly depends on local SST changes, and ΔQ_{For} the *forced* component, which is not explicitly dependent on local SST changes (e.g., wind-driven latent heat flux change). ΔQ is then broken into its net shortwave (ΔSW), upward and downward longwave (ΔLWU and ΔLWD), latent (ΔLH), and sensible (ΔSH) heat fluxes. ZL14 expressed the SST change equation as:

$$\Delta T = \frac{\Delta\text{SW} + \Delta\text{LWD} + \Delta\text{LH}_{\text{For}} + \Delta\text{SH}_{\text{For}} + \Delta O}{4\sigma[T]^3 + \gamma_1[\text{LH}] + \gamma_2[V]} \quad (1)$$

In this formulation, ZL14 treated the ΔSW and ΔLWD entirely as forcing components, with no feedback term. The ΔLWU was treated entirely as a feedback, with feedback coefficient $\alpha_{\text{LWU}} = 4\sigma[T]^3$, where σ is the Stefan–Boltzmann constant, and brackets [ ] indicate present-day values. The ΔLH feedback coefficient is $\alpha_{\text{LH}} = \gamma_1[\text{LH}]$, where $\gamma_1 = 0.06\ \text{K}^{-1}$ is obtained from the Clausius Clapeyron relation and the ΔSH feedback coefficient is $\alpha_{\text{SH}} = \gamma_2[V]$, where V is surface wind speed (see ZL14 for details). The total feedback coefficient used in ZL14 is therefore:

$$\alpha_{\text{ZL14}} = 4\sigma[T]^3 + \gamma_1[\text{LH}] + \gamma_2[V] \quad (2)$$

This framework allowed ZL14 to diagnose SST changes based on a balance between surface heat flux forcing, feedback processes, and oceanic heat adjustments.

Our sign convention is that a negative feedback (i.e., when warming induces heat fluxes out of the ocean) corresponds to a positive α value. The TIO average value of the total feedback is 15.1 $\text{W}\cdot\text{m}^{-2}\cdot{}^{\circ}\text{C}^{-1}$. α_{SH} is negligible (not shown, ZL14). α_{LH} is the largest contributor, with a TIO-averaged value of 8.9 $\text{W}\cdot\text{m}^{-2}\cdot{}^{\circ}\text{C}^{-1}$ (Figure 2c). α_{LWU} (Figure 2b) has a TIO-averaged value of 6.2 $\text{W}\cdot\text{m}^{-2}\cdot{}^{\circ}\text{C}^{-1}$ and is relatively spatially uniform across the region (Figure 2b). The spatial structure of α_{ZL14} is primarily shaped by the distribution of α_{LH} (Figures 2a and 2c). α_{LH} reflects the effects of the Clausius-Clapeyron relation, which drives evaporative cooling in response to warming. Its spatial distribution is influenced by present-day SST and wind patterns, with strongest feedback values occurring in regions of high SST and/or strong winds (not shown).

3.2. Our Refinement to ZL14

In this subsection, we present our refinements to the ZL14 framework. First, we excluded the SH feedback term for two reasons: (a) its contribution is negligible and has minimal impact on the results (not shown) and (b) the linearization of the LH flux assumes that the air-sea temperature difference remains unchanged in a future climate, implying no SST-driven change in SH fluxes. The main refinement we introduce is the inclusion of the downward longwave radiation feedback, following the analytical approach of Shakespeare and Roderick (2022, hereafter SR22). The analytical expression of its coefficient α_{LWD} is derived using equation 16 in SR22 (see SR22 for details). This approach assumes that the atmosphere adjusts to the warming of the high heat capacity ocean, resulting in a warmer, moister atmosphere with a modified vertical structure that emits more downward infrared radiation. Since changes in atmospheric temperature, humidity and vertical structure are strongly related to ΔT

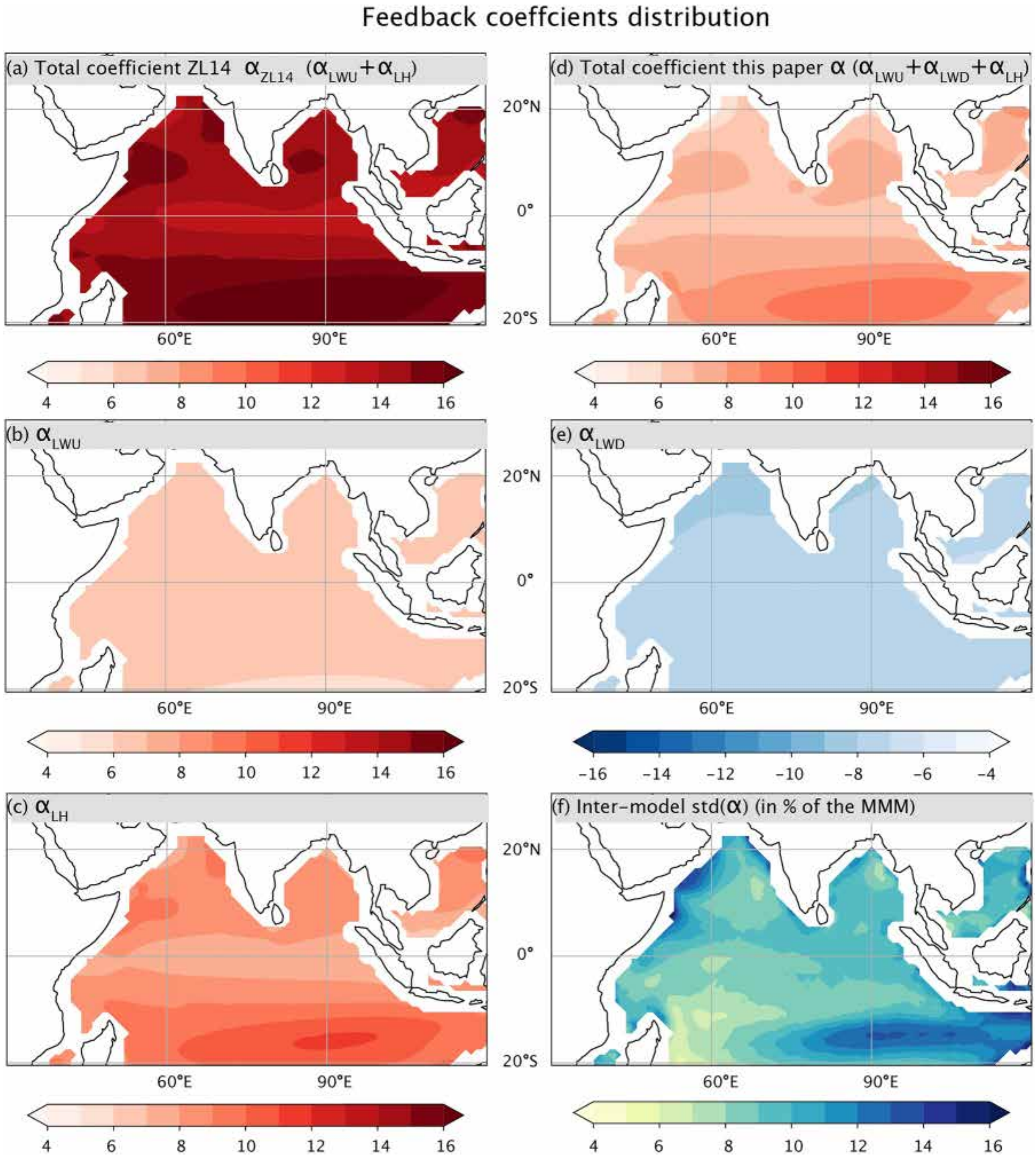

Figure 2. Air-sea heat flux feedback coefficients in CMIP5/6 models. Multi-model mean (MMM) feedback coefficients ($\mathrm{W{\cdot}m^{-2}{\cdot}{}^{\circ}C^{-1}}$): (a) Total coefficient (α_{ZL14}) from Zhang and Li (2014) (ZL14), which includes contribution from (b) latent heat flux (α_{LH}) and (c) upward longwave radiations (α_{LWU}). (d) Total coefficient (α) used in the present paper, incorporating α_{LH}, α_{LWU} and (e) downward longwave (α_{LWD}) coefficients. (f) Inter-model standard deviation of α expressed as a percentage of the MMM. Due to sign convention, feedback coefficients have opposite signs to the corresponding feedback (e.g., negative α_{LH} and α_{LWU} indicate positive feedbacks, while positive α_{LH}, α_{LWD} indicate negative feedbacks, see Equation 1 or ZL14).

(see Figure 3 in SR22), α_{LWD} is expressed as the sum of these three components. We do not include feedback effects related to changes in cloud cover, as these changes are weakly correlated to SST changes across CMIP models (see Figure 3 in SR22). The revised version of the ZL14 equation for ΔT, incorporating LWD feedback, becomes:

$$\Delta T = \frac{\Delta \mathrm{For} + \Delta O}{\alpha} = \frac{\Delta \mathrm{SW} + \Delta \mathrm{LW_{For}} + \Delta \mathrm{LH_{For}} + \Delta \mathrm{SH} + \Delta O}{\alpha} \tag{3}$$

where $\alpha = 4\sigma[T]^3 + \gamma_1[\mathrm{LH}] + \alpha_{\mathrm{LWD}}$.

Figure 2 illustrates the impact of incorporating α_{LWD} on the total feedback coefficient α. As previously noted, α_{SH} is negligible (not shown), so that $\alpha \approx \alpha_{\mathrm{ZL14}} + \alpha_{\mathrm{LWD}}$. The feedbacks we have discussed so far (LH, LWU) are negative feedbacks, but the LWD feedback is positive (expressed as negative α_{LWD} under our sign convention, Figure 2e) with a basin-averaged value of $-7.5\ \mathrm{W{\cdot}m^{-2}{\cdot}{}^{\circ}C^{-1}}$. This negative α_{LWD} largely offsets the positive α_{LWU}, reducing the basin-averaged total coefficient from $15.1\ \mathrm{W{\cdot}m^{-2}{\cdot}{}^{\circ}C^{-1}}$ in ZL14 to $7.6\ \mathrm{W{\cdot}m^{-2}{\cdot}{}^{\circ}C^{-1}}$ in our study (Figures 2c and 2f). Similar to its upward counterpart, the LWD feedback coefficient has little spatial variation. As a result, the spatial pattern of α is primarily determined by α_{LH}, with a clear equatorial minimum (Figures 2c and 2d). Overall, incorporating the downward longwave feedback reduces the total feedback coefficient by half relative to ZL14 and increases the relative importance of spatial variations. Figure 2f finally displays the inter-model standard deviation of α, expressed as a percentage of the MMM value. α exhibits relatively small inter-model variability, with deviations of less than 10% of the MMM value in the equatorial region and up to 15% near the western Arabian Sea coast and in the southeastern Indian Ocean near 15°S.

3.3. Equations for Changes in Basin-Averaged SST and RSST

From Equation 3, we derive expressions for the basin-averaged ΔT ($\overline{\Delta T}$) and for deviations from the basin-mean change ($\Delta T'$). The detailed derivations are provided in Appendix A. To simplify the formulation, we approximate the feedback coefficient α by its MMM value, $<\alpha>$, justified by the relatively small inter-model coefficient diversity α'. We verified that this approximation yields comparable results to exact computations. The equation for $\overline{\Delta T}$ is:

$$\overline{\Delta T} = \frac{\overline{\Delta For} + \overline{\Delta O}}{\langle \alpha \rangle} \tag{4}$$

where the overbar ($^{-}$) designates averaging over the TIO region and angle brackets (<>) indicate the MMM value. The contribution of individual flux components to ΔQ_{for} term can be further broken down as shown in Equation 3. The equation for $\Delta T'$ follows:

$$\Delta T' = \frac{\Delta \mathrm{For}' + \Delta O' - \alpha' \overline{\Delta T}}{\langle \alpha \rangle} \tag{5}$$

In this equation, $\alpha' \overline{\Delta T}$ represents the contribution of the spatial inhomogeneity of the total feedback coefficient to $\Delta T'$ (e.g., the fact that reduced negative feedback from evaporative cooling in climatologically colder regions results in less warming, as discussed in e.g. Xie et al., 2010).

To quantify the contribution of each process to the inter-model diversity of $\overline{\Delta T}$ or $\Delta T'$, we express the variance of these quantities as the sum of the covariances between each term on the right-hand side of Equations 4 and 5 with $\overline{\Delta T}$ and $\Delta T'$, respectively. The detailed derivation of this variance decomposition is provided in Appendix B.

As with the original ZL14 equation (not shown), Equation 4 accurately reproduces the $\overline{\Delta T}$ in CMIP5/6 models, with the reconstructed MMM differing by less than 1% from the actual CMIP5/6 value and an inter-model correlation of 0.92 (Figure 3a). Similarly, the $<\Delta T'>$ pattern reconstructed from Equation 5 matches the CMIP5/6 MMM, with a pattern correlation of 0.99 (Figure 3b; comparing contours and shading). Figures 3c and 3d further indicates that Equation 5 accurately captures the inter-model diversity in $\Delta T'$, with correlations of 0.97 and 0.95 for the zonal (ZGRAD) and meridional (MGRAD) SST gradients, respectively.

4. Basin-Average Warming

In this section, we will use Equation 4 to explore the drivers of the CMIP5/6 TIO-average warming ($\overline{\Delta T}$). We first discuss the MMM (Section 4.1) and then investigate the inter-model spread (Section 4.2).

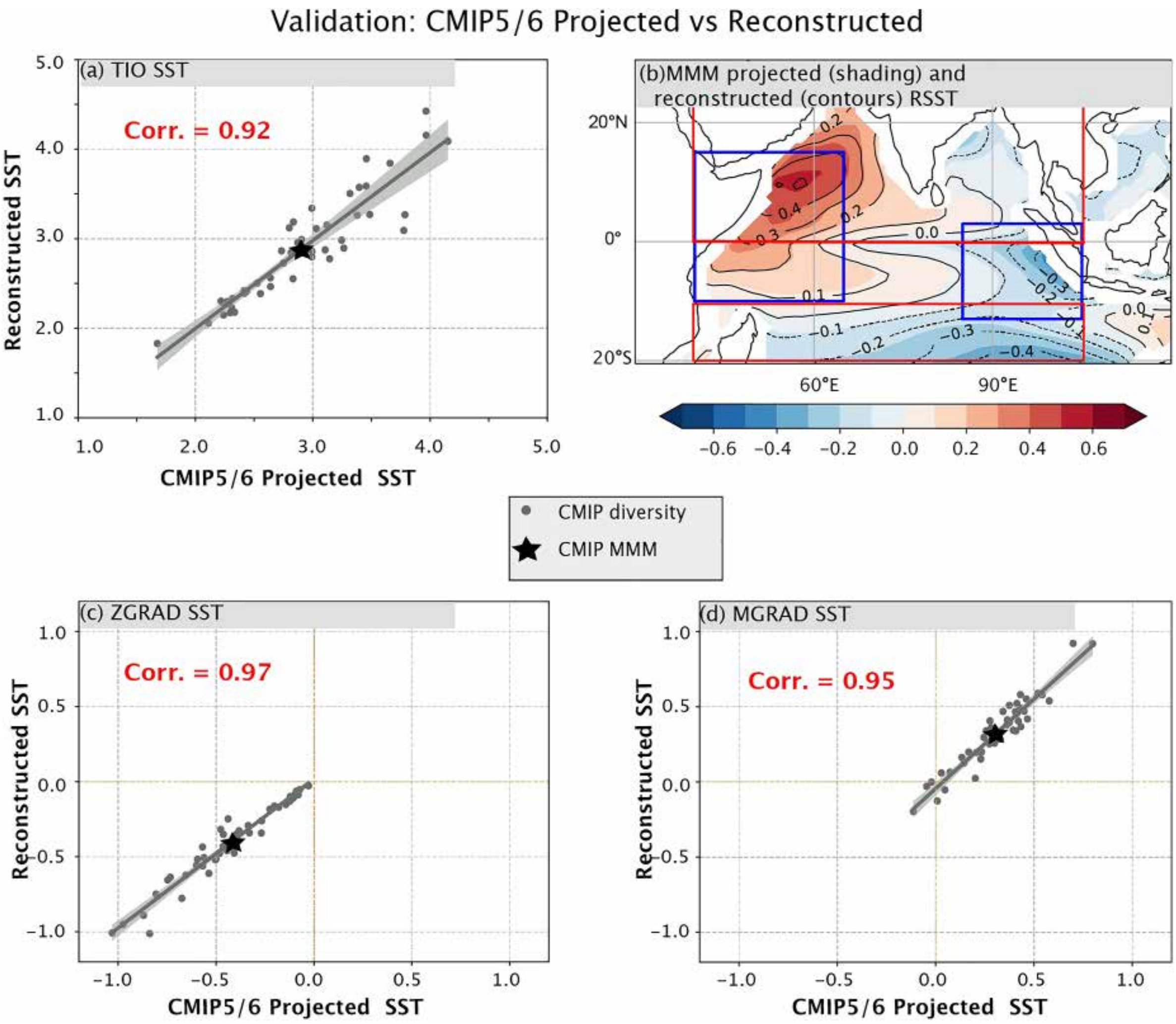

Figure 3. Comparison between reconstructed versus CMIP5/6 projected basin-averaged warming ($\overline{\Delta T}$) and Relative SST (RSST, $\Delta T'$) patterns. (a) Scatterplot of $\overline{\Delta T}$ reconstructed using Equation 4 versus Coupled Model Intercomparison Project (CMIP) projected values. (b) $<\Delta T'>$ from CMIP data set (shading) and reconstructed values using Equation 5 (contours). Scatterplots of the reconstructed versus CMIP $\Delta T'$ for the (c) zonal SST gradient (ZGRAD) and (d) meridional SST gradient (MGRAD). Blue boxes on panel (b) indicate the West Indian Ocean and East Indian Ocean regions used to compute ZGRAD, while red boxes on panel (b) indicate the North and South regions used to compute MGRAD. Each gray dot on panels (a), (c), and (d) represents an individual model, with the black star indicating the multi-model mean. The gray line represents the least-square regression slope, with the 95% confidence interval shown as a light gray shading. Correlation values are displayed in red.

4.1. Drivers of MMM Basin-Average Warming

The MMM TIO-average warming, $<\overline{\Delta T}>$, is slightly below 3°C and primarily driven by the SST-independent part of the surface net heat flux change, $<\overline{\Delta \mathrm{For}}>$. The ocean dynamics contribution $<\overline{\Delta O}>$ is negligible (Figure 4a). The net surface flux forcing is further decomposed into its four components. ZL14 identified downwelling longwave radiation forcing, $<\overline{\Delta \mathrm{LWD}_{\mathrm{For}}}>$, as the dominant contributor to the TIO-averaged warming. In ZL14, the entire TIO-average MMM LWD change (28.5 Wm^{-2}) was treated as a forcing term. In our study, however, a large fraction of this change (21.7 Wm^{-2}) is accounted for by the downwelling longwave radiative feedback term, $-\alpha_{\mathrm{LWD}} < \Delta T>$, reducing the downwelling longwave radiation forcing by 76% compared to ZL14. As a result, the contribution of downward longwave forcing to the MMM TIO-averaged SST change is much smaller in our study than in ZL14 (Figure 4a). The dominant contributor is the basin-averaged latent heat flux forcing, $<\overline{\Delta \mathrm{LH}_{\mathrm{For}}}>$, accounting for ~78% of the total warming. $<\overline{\Delta \mathrm{LW}_{\mathrm{For}}}>$ contribute to 30%, $<\overline{\Delta \mathrm{SH}}>$ 9% and $<\overline{\Delta \mathrm{SW}}>$ −9% of $\overline{\Delta T}$. The TIO average warming and its contributors do not vary across seasons (not shown).

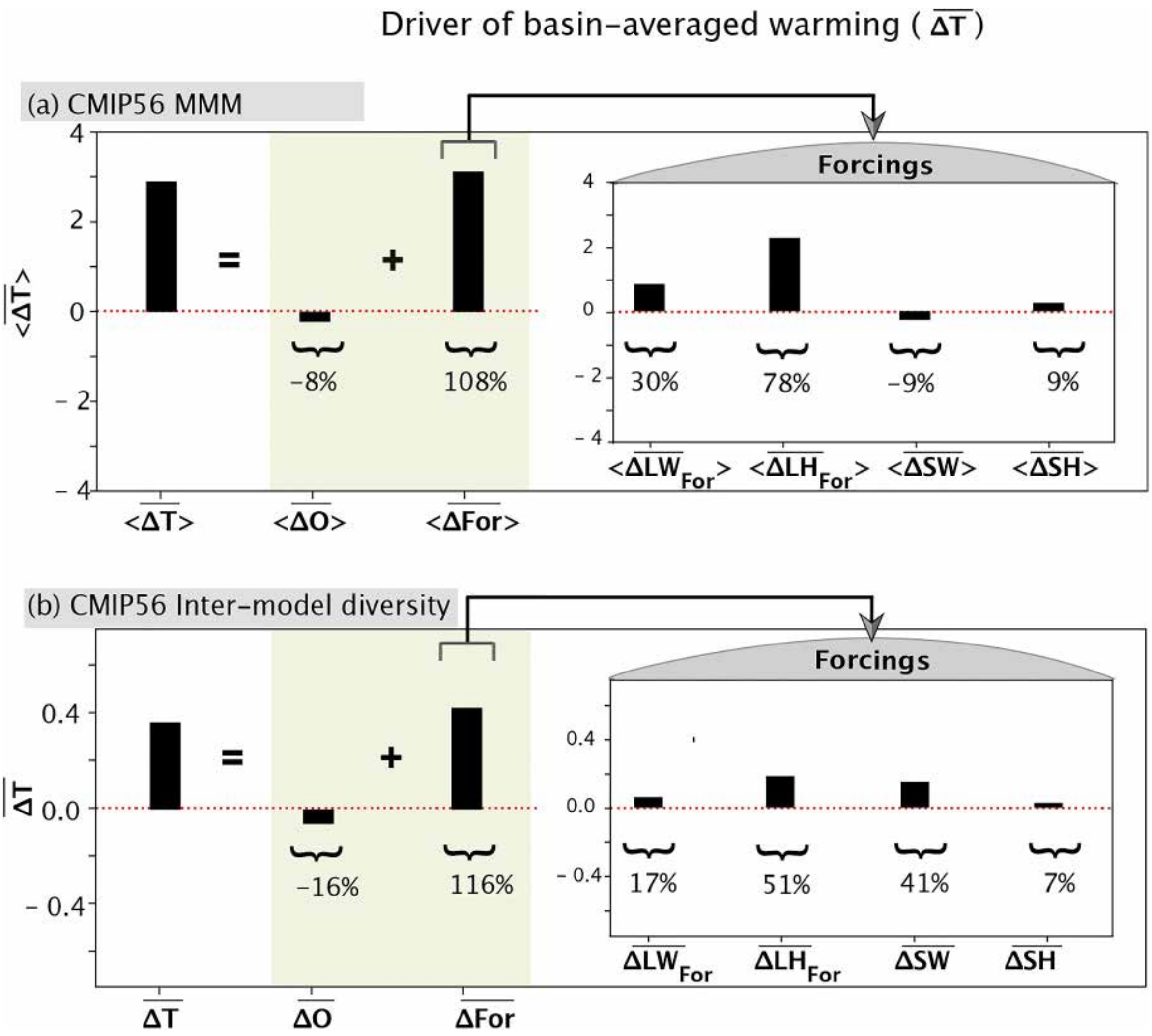

Figure 4. Drivers of the basin-averaged warming multi-model mean (MMM) ($\langle\overline{\Delta T}\rangle$) and of its inter-model diversity ($\overline{\Delta T}$). (a) MMM basin-averaged warming $\langle\overline{\Delta T}\rangle$ from Equation 4, and contributions from changes in ocean dynamics ($\langle\overline{\Delta O}\rangle$) and changes atmospheric forcing ($\langle\overline{\Delta \mathrm{For}}\rangle$). $\langle\overline{\Delta \mathrm{For}}\rangle$ is further decomposed in forcing contributions from longwave radiation ($\langle\overline{\Delta LW_{For}}\rangle$), latent heat flux ($\langle\overline{\Delta LH_{For}}\rangle$), shortwave radiation ($\langle\overline{\Delta SW}\rangle$) and sensible heat flux ($\langle\overline{\Delta SH}\rangle$). (b) Decomposition of the inter-model variance in $\overline{\Delta T}$ from Equation 4 into the contributions from $\overline{\Delta O}$, $\overline{\Delta \mathrm{For}}$ and its four components. The percentage indicated shown below each bar represent the relative contribution of each term to $\overline{\Delta T}$.

Linearizing the bulk formula indicates that latent heat flux forcing depends on wind speed and near-surface relative humidity changes (e.g., ZL14). Figures 5a and 5b displays changes in surface wind speed and relative humidity, respectively, with $\langle\Delta LH_{For}\rangle$ overlaid as contours. The pattern correlation between $\langle\Delta LH_{For}\rangle$ and wind changes is −0.69, while its correlation with the relative humidity change is 0.70, suggesting that both factors contribute comparably to $\langle\Delta LH_{For}\rangle$ MMM changes. The increase in relative humidity (Figure 5b) leads to more saturated near-surface air, which suppresses surface contributing positively to $\langle\Delta LH_{For}\rangle$. The basin-wide windspeed reduction leads to reduced evaporative cooling, with the largest decrease occurring over the Arabian Sea, the southern Bay of Bengal and the southeastern TIO. As illustrated in Figure 6, the MMM wind reduction reflects a weakening of both the summer and winter monsoonal circulations, with wind changes (Figures 6b and 6e) generally opposing their present-day climatology (Figures 6a and 6d). Inter-model regressions to the basin-average latent heat forcing $\langle\Delta LH_{For}\rangle$ (Figures 6c and 6f) indicate that the southern hemisphere wind reduction dominates in summer, while the northern hemisphere contributes most in winter.

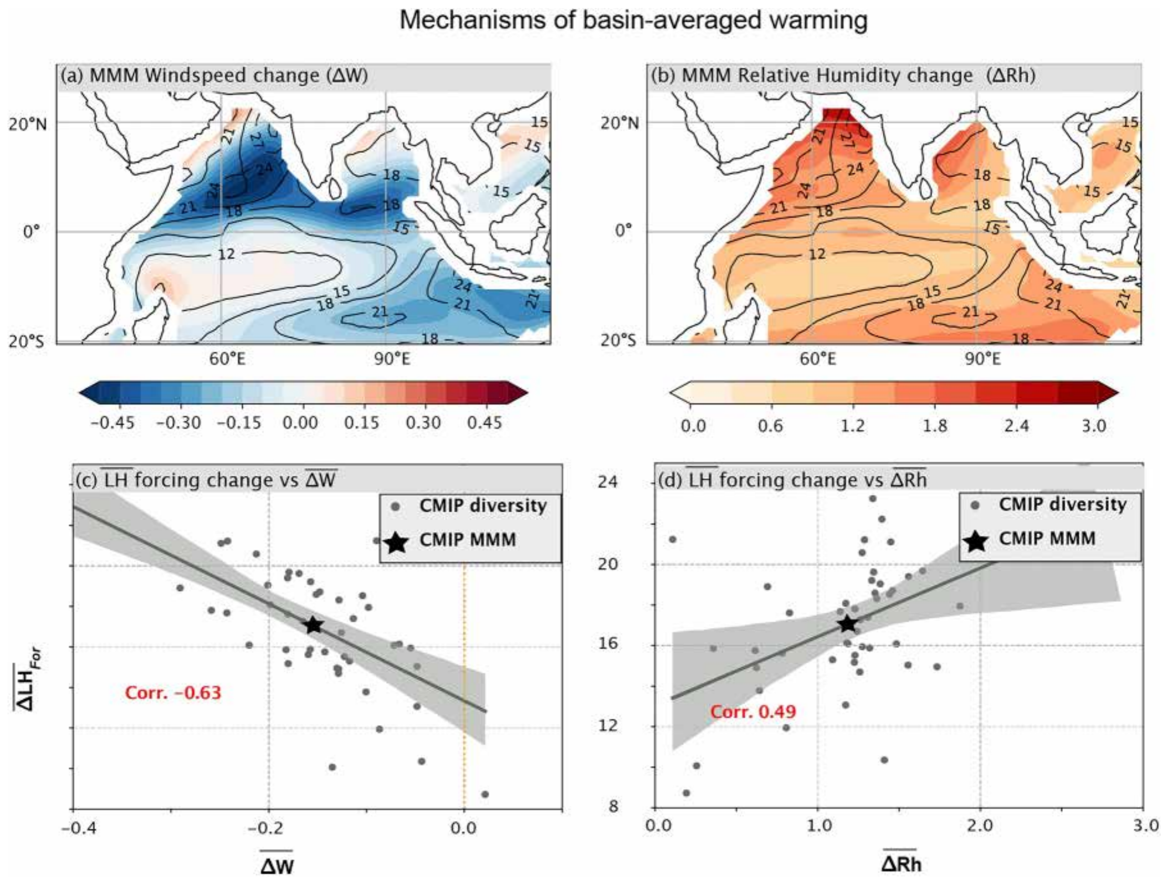

Figure 5. Factors controlling TIO latent heat flux forcing. (a) Multi-Model Mean (MMM) wind speed (ΔW) and (b) relative humidity (ΔRh) changes (shading), with latent heat flux forcing changes overlaid as contours. (c) Relationship between basin-averaged latent heat flux forcing and wind speed changes (ΔW) ($m{\cdot}s^{-1}$) across Coupled Model Intercomparison Project models. (d) Relationship between basin-averaged latent heat flux forcing and relative humidity (ΔRh) (%). Each dot represents an individual model, and stars indicate the MMM. The gray line represents the least-square regression slope, with the 95% confidence interval shown as a light gray shading. Correlation values are displayed in red.

4.2. Drivers of Basin-Average Warming Diversity

Figure 4b shows the decomposition of inter-model variance in $\overline{\Delta T}$ into contributions from the terms in Equation 4. Consistent with the MMM results, the inter-model diversity in $\overline{\Delta T}$ is primarily driven by $\overline{\Delta \mathrm{For}}$, with a minor opposing contribution from oceanic processes. Breaking down the atmospheric forcing further reveals that the largest contributor is $\overline{\Delta \mathrm{LH}_{\mathrm{For}}}$ (51%), followed by $\overline{\Delta \mathrm{SW}}$ (41%), with smaller contributions from $\overline{\Delta \mathrm{LW}_{\mathrm{For}}}$ (17%) and $\overline{\Delta \mathrm{SH}}$ (7%). As for the MMM, the level of warming induced by $<\Delta \mathrm{LH}_{\mathrm{For}}>$ is predominantly controlled by the magnitude of the wind speed reductions across models (correlation of −0.63, Figure 5c). The amplitude of this wind reduction reflects the impact of the summer monsoon winds on evaporation in the southern hemisphere, and that of the winter monsoon in the northern hemisphere (Figures 6e and 6f). In other words, the summer and winter monsoon weakening intensities both contribute to the inter-model diversity in TIO-average warming. Relative humidity also contributes to $<\Delta \mathrm{LH}_{\mathrm{For}}>$ but to a lesser extent (correlation of 0.49, Figure 5d). These two factors, windspeed reduction and relative humidity increase, are largely independent (correlation of −0.11), and their combined effect in a bi-linear regression model raises the correlation to 0.76. In addition, shortwave radiation changes are related to cloud cover changes, with a correlation of −0.64 (Figure S2 in Supporting Information S1). Enhanced warming over the western IO leads to increased cloud fraction and decreased shortwave radiation, whereas the eastern and southern IO experience a decrease in cloud fraction and a comparatively weaker increase in shortwave radiation. As for the MMM, diversity in the warming magnitude and their related drivers remain consistent across seasons (not shown).

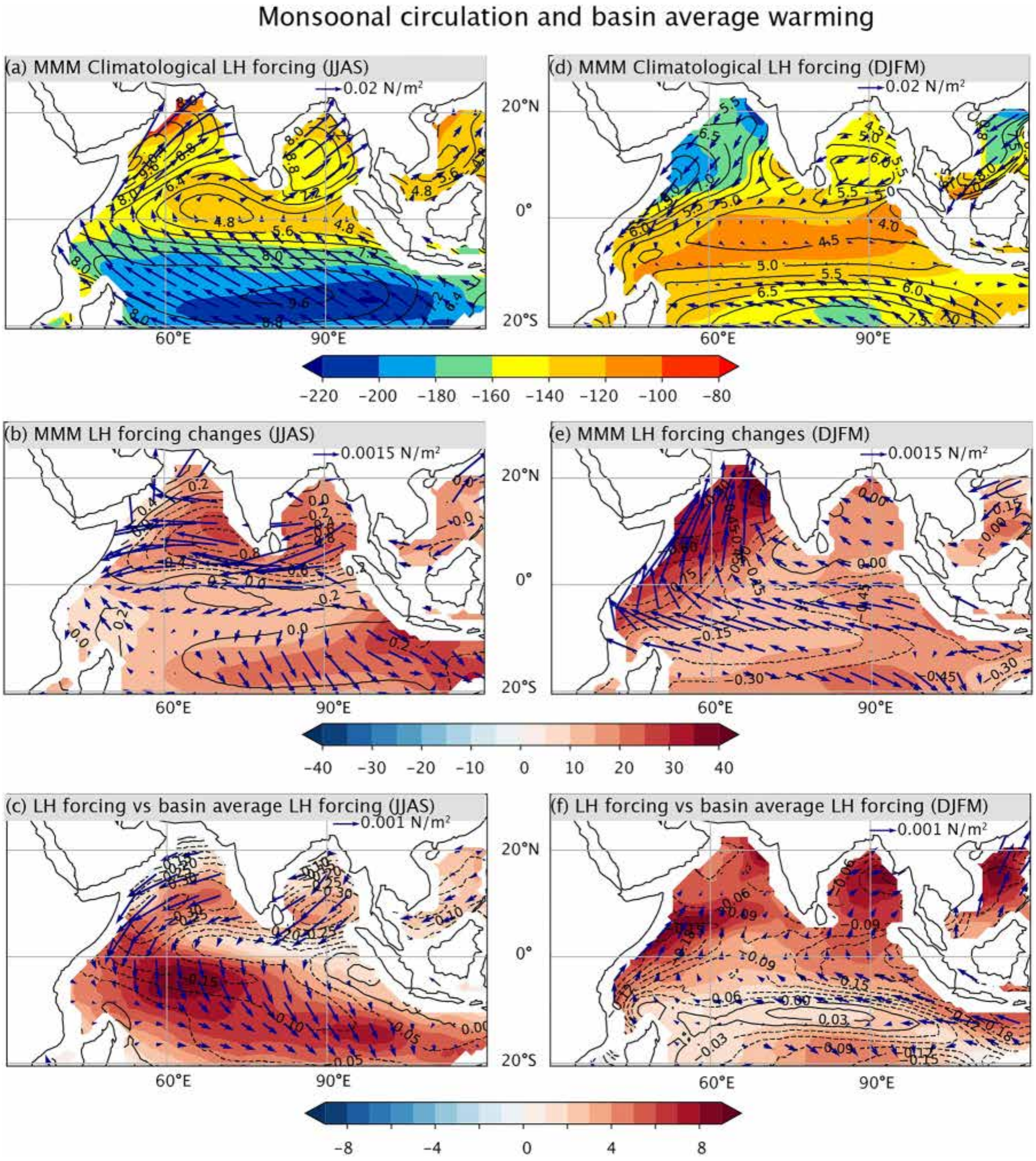

Figure 6. Annual circulation slowdown related to seasonal monsoonal circulation reduction. Multi-model mean latent heat forcing (shading), windspeed (contours) and windstress (arrows). (a and b) Climatology and (c and d) changes in summer (JJAS) and winter (DJFM), respectively. (e and f) Linear regression of latent heat flux forcing (shading), windspeed (contours) and wind stress (arrows) changes onto basin-averaged latent heat flux forcing across Coupled Model Intercomparison Project models for summer and winter, respectively.

In summary, there are three key drivers of the inter-model diversity in the basin-averaged TIO warming. The slowdown of the summer and winter monsoonal circulations and increase in near-surface relative humidity operate through their influence on evaporative cooling, and cloud cover changes through their impact on shortwave heat fluxes. In contrast, the direct effect of the greenhouse gases on the net surface longwave flux changes plays a much smaller role, underlining the importance of latent heat forcing in determining the basin-averaged warming amplitude.

5. Warming Patterns

This section examines the mechanisms driving the TIO warming pattern in CMIP models. Section 5.1 identifies two key features of the projected $\Delta T'$ pattern: changes in the zonal equatorial SST gradient (IOD-like warming) and the interhemispheric gradient, both of which contribute to inter-model diversity. Section 5.2 analyses the drivers of these patterns using Equation 5, considering both the MMM response and inter-model diversity.

5.1. Main Features of Inter-Model Diversity

The largest $\Delta T'$ inter-model variations occur in the western TIO, particularly off the coasts of Somalia and Oman, and in the equatorial eastern Indian Ocean and southern Indian Ocean, near Java and Sumatra (Figure 7a). In these regions, the standard deviation represents a substantial fraction of the MMM change. To identify dominant modes of inter-model diversity in $\Delta T'$ patterns, we perform an Empirical Orthogonal Function (EOF) analysis across CMIP models. The first EOF, accounting for 29% of the total variance, reveals a distinct zonal contrast between the western and eastern TIO (Figure 7b). The associated inter-model diversity in wind stress changes, obtained by regressing wind stress anomalies on the normalized principal component, shows equatorial easterly wind anomalies, flowing from negative to positive $\Delta T'$ regions (Figure 7b). This pattern closely resembles the MMM wind changes and IOD-like warming pattern (Figure 1a). The -0.74 correlation with the first principal component indicates a robust link between the IOD-like warming amplitude and equatorial easterly wind stress changes (Figure 7c). The second EOF mode explains 22% of the variance and displays a north-south $\Delta T'$ dipole (Figure 7d). The associated inter-model diversity in wind stress changes features southerly wind anomalies, flowing from negative to positive $\Delta T'$ regions (Figure 7d). The 0.75 correlation with the second principal component indicates a close relationship between the interhemispheric $\Delta T'$ gradient strengthening and the cross-equatorial change (Figure 7e). Both winter and summer monsoon meridional wind stress changes contribute equally to this relationship (Figure S3 in Supporting Information S1). The two leading modes (51% of variance) of inter-model diversity can be described as amplitude modulations of the (a) MMM IOD-like warming and associated zonal circulation slowdown and (b) interhemispheric temperature gradient and associated cross-equatorial circulation changes.

5.2. Drivers of the TIO Warming Pattern

Figure 8 displays the contributions of individual processes to the MMM $\Delta T'$ change, $<\Delta T'>$, as derived from Equation 5. $<\Delta O'>$ exhibits an east-west equatorial $\Delta T'$ dipole that matches the projected $<\Delta T'>$ pattern (Figure 8b). In contrast, $<\Delta \mathrm{For}'>$ (Figure 8a), primarily driven by $<\Delta \mathrm{LH}'_{\mathrm{For}}>$ and $<\Delta \mathrm{SW}'>$ (Figures 8e and 8f), largely mirrors $<O'>$ but with the opposite sign. The inhomogeneity of the feedback coefficient, $\alpha' \overline{\Delta T}$, warm the northern hemisphere and cool the southern hemisphere (Figure 8c). This hemispheric asymmetry is linked to a stronger latent feedback coefficient leading to less warming in the southern hemisphere (Figures 2c and 2d). Overall, this analysis indicates that oceanic processes drive the MMM IOD-like warming pattern, while atmospheric forcing opposes this change. Meanwhile, interhemispheric asymmetries in the feedback coefficient drive the MMM interhemispheric SST gradient strengthening.

5.3. Drivers of the Zonal Equatorial SST Gradient Change (IOD-Like Warming)

Given the equatorial zonal SST gradient (ZGRAD) influence on the Walker Cell, we first focus on processes governing its change (blue frames on Figure 7b). We do not detail changes in the eastern and western TIO boxes, as they largely mirror each other (not shown). Consistent with Figure 8, the ZGRAD reduction is predominantly attributable to $<\Delta O'>$, while $<\Delta \mathrm{For}'>$ opposes this change (Figure 9a). This opposing contribution is mainly driven by $<\Delta \mathrm{SW}'>$ and to a lesser extent $<\Delta \mathrm{LH}'_{\mathrm{For}}>$. The heterogeneity of the feedback coefficient, specifically the weaker negative evaporative feedback in the climatologically colder western Indian Ocean, also modestly contributes to $<\Delta T'>$.

Figure 9b shows the decomposition of the ZGRAD inter-model variance into contributions from the different terms in Equation 5. Similar to the MMM results, ZGRAD inter-model diversity is driven by differences in $\Delta O'$, with the spatial heterogeneity of the feedback coefficient playing a secondary role. $\Delta \mathrm{For}'$ generally opposes the gradient change.

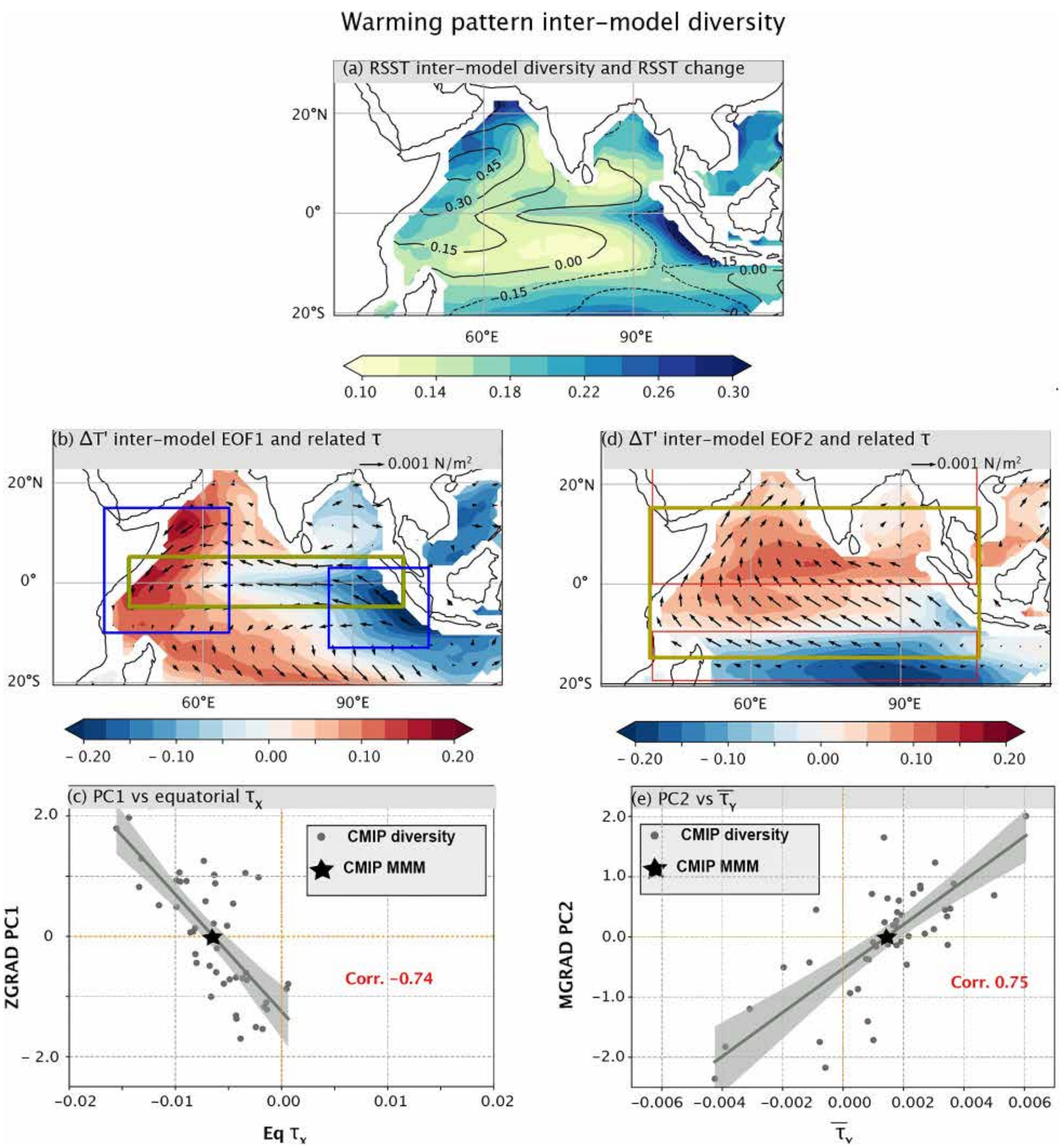

Figure 7. Warming pattern inter-model diversity and its drivers. (a) $\Delta T'$ standard deviation (shading) across Coupled Model Intercomparison Project models and multi-model mean $\Delta T'$ (contour). (b) First and (d) second EOF mode of $\Delta T'$ (computed across the model space, shading) and associated wind stress signals (vectors) obtained through linear regression to the associated normalized principal component PC1 and PC2, respectively. (c) Scatterplot of the normalized PC1 versus the average zonal wind stress change in the Equatorial box (45°−100°E; 5°S–5°N) displayed as a yellow frame on panel (b). (e) Scatterplot of the normalized PC2 versus the average meridional wind stress change 40°−105°E; 15°S–15°N domain displayed as a yellow frame on panel (d). The gray line represents the least-square regression slope, with the 95% confidence interval shown as a light gray shading. Correlation values are displayed in red.

Figures 10a and 10b highlights the mechanisms determining the amplitude of the IOD-like warming across CMIP models. Following the "warmer-get-wetter" paradigm, a negative ZGRAD ($\Delta T'$ warming in the west and cooling in the east) intensifies convection in the west and suppresses it in the east (Figure 10a), with an inter-model correlation of 0.86 (Figure 10b). The Gill response to this east-west convective dipole consists of equatorial easterly changes (0.86 correlation). The equatorial Sverdrup balance implies a thermocline deepening in the

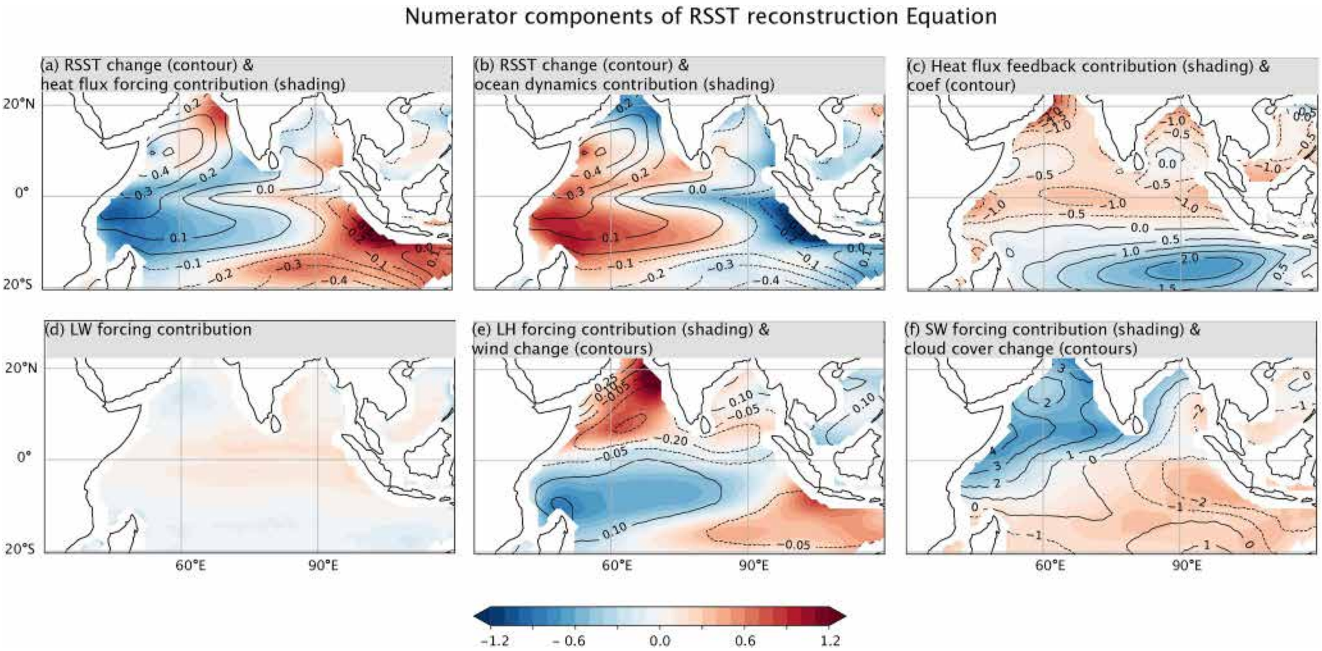

Figure 8. Drivers of multi-model mean (MMM) warming pattern. Contributions to $<\Delta T'>$ from (a) surface heat flux forcing ($<\Delta \mathrm{For}'>$), (b) oceanic processes ($<\Delta O'>$) and (c) heat flux feedback coefficient ($\alpha' \overline{\Delta T}$). Contours represent $<\Delta T'>$ (°C) in panels (a) and (b) and α' ($\mathrm{W{\cdot}m^{-2}{\cdot}K^{-1}}$) in panel (c). The surface heat flux forcing in panel (a) is further decomposed into contributions from (d) net longwave radiation ($<\Delta \mathrm{LW}'>$), (e) latent heat flux ($<\Delta \mathrm{LH}_{\mathrm{for}}>$, shading), with MMM windspeed change ($\mathrm{m{\cdot}s^{-1}}$) overlaid as contours, and (f) shortwave radiation ($<\Delta \mathrm{SW}'>$, shading), with MMM cloud cover (%) overlaid as contours.

western TIO and shoaling in the east, in response to these equatorial easterly changes (correlation of 0.92). The thermocline feedback implies enhanced cooling through oceanic processes in the east and reduced cooling in the west (inter-model correlation of 0.83). The 0.71 correlation between changes in the $\Delta O'$ zonal gradient and $\Delta T'$ closes the feedback loop. This positive feedback loop on the zonal SST gradient is characteristic of the Bjerknes feedback.

There is also a stabilizing negative feedback from shortwave fluxes. A stronger IOD-like pattern yields an increased rainfall and cloudiness dipole, strengthening the shortwave flux dipole (−0.86 correlation) and ZGRAD damping (−0.60 correlation). The strong correlations at each step of these feedback loops illustrate the Bjerknes feedback pivotal role in setting the IOD-like warming amplitude, with shortwave fluxes acting as a damping process. While these feedback mechanisms can adjust the level of ZGRAD changes, they do not explain the initial trigger which starts weakening ZGRAD. We will discuss potential trigger mechanisms in Section 6.

Unlike the basin-wide warming, ZGRAD changes display a seasonal modulation (Figure S1 in Supporting Information S1), with the strongest MMM IOD-like warming and inter-model diversity in summer and fall. During these seasons, the thermocline is climatologically shallower in the eastern TIO, amplifying the efficiency of the Bjerknes feedback loop (not shown).

5.4. Drivers of the Inter-Hemispheric SST Gradient Change

We then turn our focus on the meridional SST gradient (MGRAD; red frames on Figure 7d) changes, given its importance in shaping the Hadley Cell, Intertropical Convergence Zone, monsoonal circulation and rainfall. Consistent with Figure 8, the MMM MGRAD strengthening is predominantly driven by the inhomogeneity of the feedback coefficient (Figure 11a), $<\alpha' \overline{\Delta T}>$, due to a stronger negative evaporative feedback in the southern Indian Ocean, where winds are climatologically stronger (Figure 2). $<\Delta \mathrm{For}'>$ generally opposes this change (Figure 11a), mainly through shortwave radiation changes, because cloudiness increases in the northwestern Indian Ocean due to the warmer get wetter mechanism.

Figure 11b shows the decomposition of the MGRAD inter-model variance into contributions from the different terms in Equation 5. In contrast to the MMM results, MGRAD inter-model diversity is mainly attributable to the

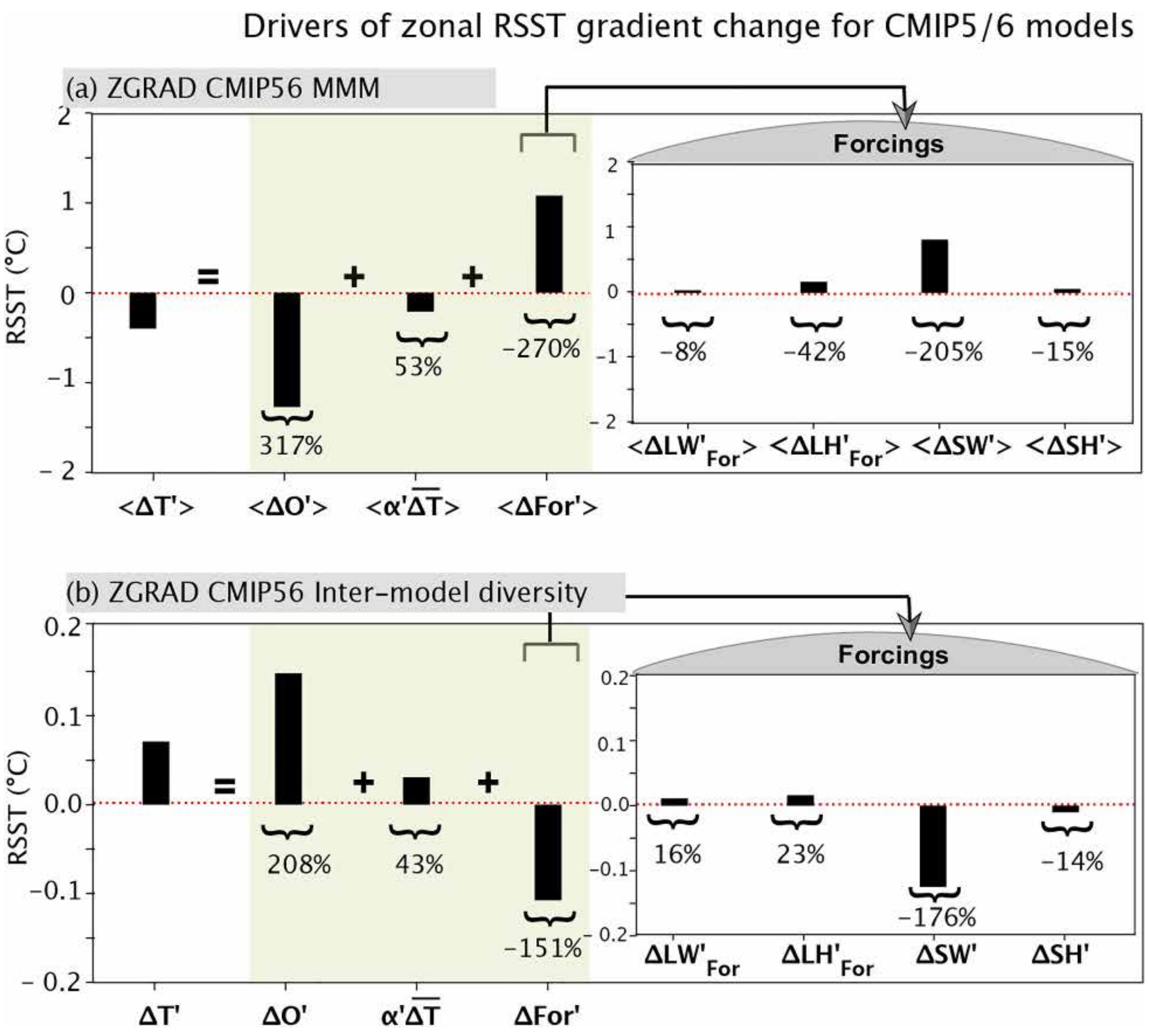

Figure 9. Drivers of the projected zonal equatorial $\Delta T'$ gradient change (ZGRAD) multi-model mean (MMM) and of its inter-model diversity. (a) MMM ZGRAD, defined as the difference between $\Delta T'$ changes in the WIO and EIO (see regions in Figure 6a), and contributions from changes in ocean dynamics ($<\Delta O'>$), feedback coefficient inhomogeneity ($<\overline{T}\alpha'>$) and atmospheric forcing ($<\Delta \mathrm{For}'>$). $<\Delta \mathrm{For}'>$ is further decomposed into forcing contributions from longwave radiation ($<\Delta \mathrm{LW}'_{\mathrm{For}}>$), latent heat flux ($<\Delta \mathrm{LH}'_{\mathrm{For}}>$), shortwave radiation ($<\Delta \mathrm{SW}'>$) and sensible heat flux ($<\Delta\overline{\mathrm{SH}}>$), shown in a separate box. (b) Decomposition of the inter-model variance in ZGRAD into contributions from $\Delta O'$, $\overline{T}\alpha'$, $\Delta \mathrm{For}'$, along with its four components. The percentages shown below each bar represent the relative contribution of each term to ZGRAD.

differences in $\Delta \mathrm{For}'$, with the diversity in $\alpha'\overline{\Delta T}$ playing a much weaker role, and $\Delta O'$ resisting the change. $\Delta \mathrm{LH}'_{\mathrm{For}}$ is the largest contributor to the diversity in $\Delta \mathrm{For}'$. MGRAD has a weaker seasonal modulation than ZGRAD (not shown).

Figures 10c and 10d illustrates the mechanisms driving the strengthening of MGRAD in CMIP models. On average, this gradient is setup by a differential interhemispheric evaporative feedback, linked to stronger climatological winds in the southern compared to the northern TIO. This feedback results in $\Delta T'$ cooling in the south and warming in the north, which induces southerly cross-equatorial wind anomalies of varying magnitude across CMIP models (0.73 correlation). Stronger cross-equatorial wind anomalies amplify windspeeds in the southern TIO (0.54 correlation), increasing latent heat cooling (−0.74), which cools the southern hemisphere (0.47) and strengthens the MGRAD (−0.96). Simultaneously, stronger southerly winds decrease the southward transport of dry continental air by the winter monsoon, increasing northern Indian Ocean relative humidity (0.50).

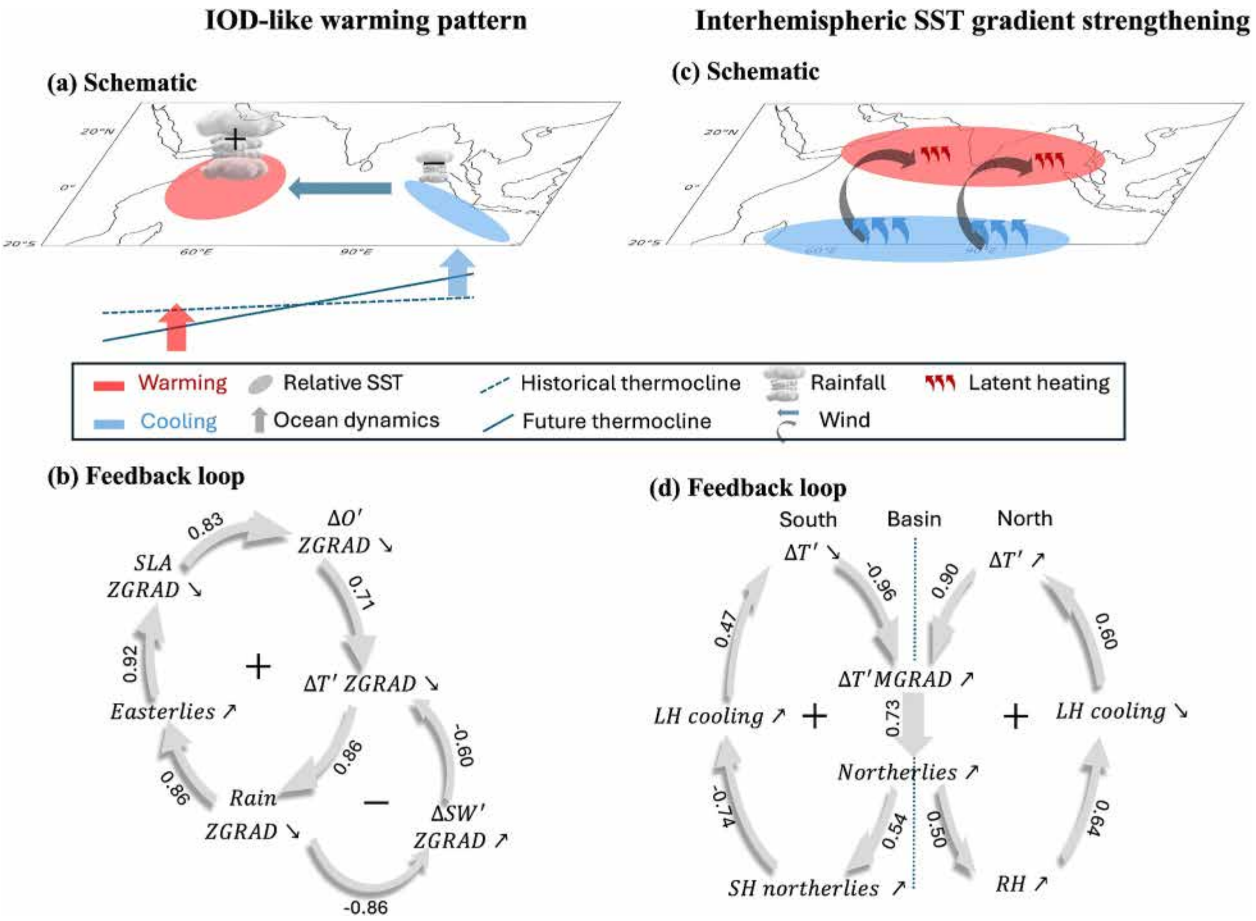

Figure 10. Mechanisms driving the two dominant warming patterns in the TIO. (a) Schematics representation of the processes driving the IOD-like warming pattern and (b) the associated feedback loop. Correlations along the feedback loop indicate inter-model relationships between variables. The sign of the feedback is indicated in the center of the loop. (c and d) Similar schematic and feedback loop for the strengthening of the interhemispheric SST gradient.

This higher relative humidity reduces latent heat cooling (0.64), enhancing the northern hemisphere warming (0.60), and strengthening MGRAD (0.90). The lowest correlation above (0.47) is significant at the 99.9% level, indicating a robust feedback loop, although less robust than that for ZGRAD.

These results indicate that the trigger of the MMM interhemispheric temperature gradient strengthening is the stronger southern hemisphere evaporative cooling, in relation to stronger winds. A feedback loop between the interhemispheric gradient change, winds and evaporation further controls the MGRAD inter-model diversity. This feedback loop involves wind changes in both hemispheres, a modulation of latent heat flux forced by windspeed in the south and relative humidity variations in the north.

6. Summary and Discussion

The magnitude and spatial pattern of the TIO warming play a crucial role in shaping regional climate and atmospheric circulation changes. This study investigates the mechanisms driving TIO warming using projections from 46 CMIP5/6 models under unmitigated emissions, applying an upper ocean heat budget framework adapted from Zhang and Li (2014). By assessing contributions from oceanic processes, SST-independent heat flux forcing, and SST-dependent heat flux feedback, we refine the understanding of TIO warming drivers. Beyond the basin-wide warming, our analysis highlights two distinct warming patterns that together explain half of the total inter-model RSST variance: the zonal equatorial “IOD-like” warming pattern (Cai et al., 2014) and a less-documented modulation of the interhemispheric SST gradient.

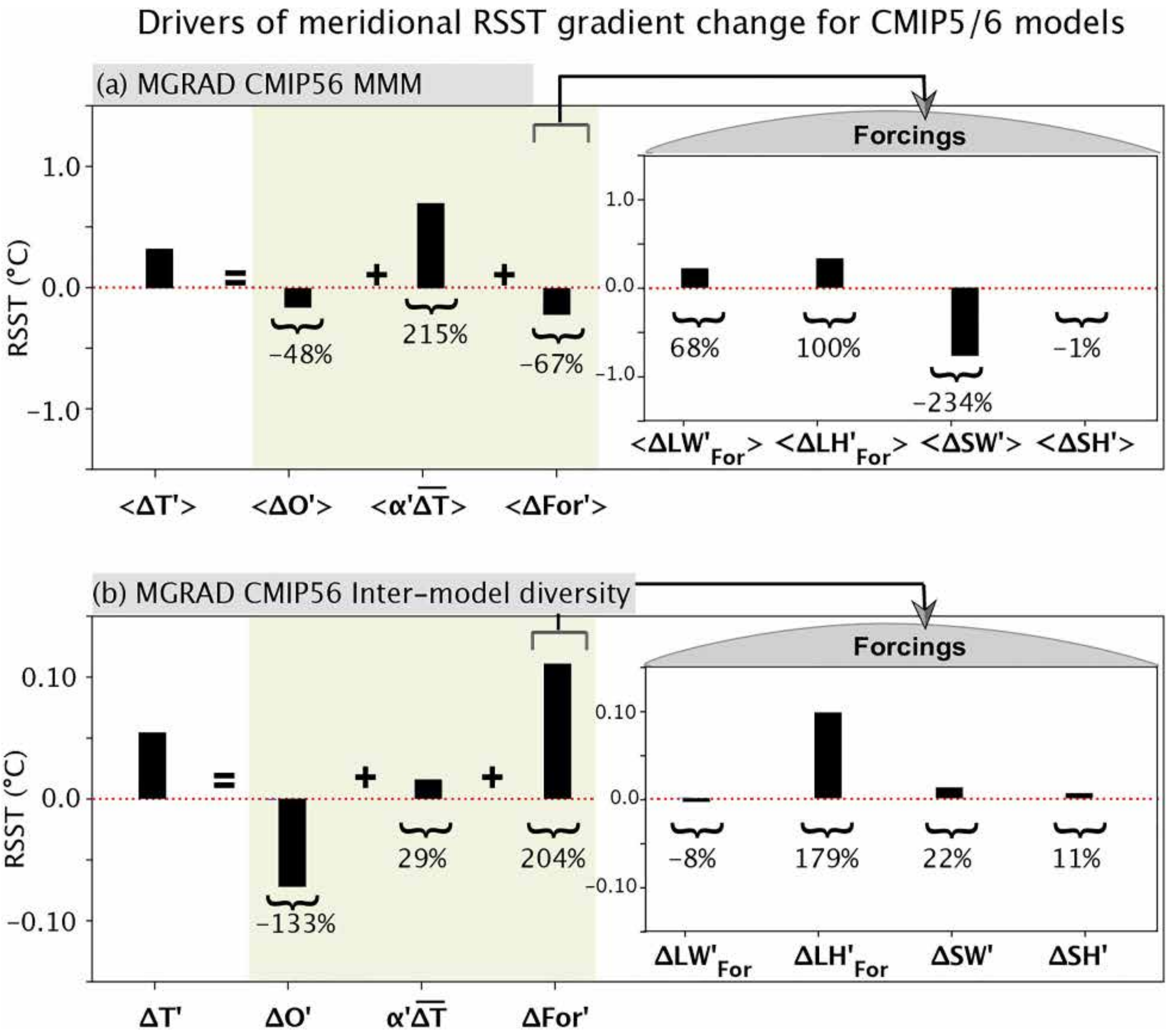

Figure 11. Drivers of the projected meridional interhemispheric $\Delta T'$ gradient change (MGRAD) multi-model mean and of its inter-model diversity. Same as Figure 9 but for MGRAD instead of ZGRAD.

Zhang and Li (2014) primarily attributed warming to downward longwave, treating it entirely as a forcing. In contrast, we apply recent analytical advances, which attribute most of the downward longwave change to a positive feedback linked to SST-driven atmospheric warming and moistening (Shakespeare & Roderick, 2022). Consequently, we find a smaller role for downward longwave radiation than ZL14. Instead, our results rather indicate that latent heat flux forcing dominates the MMM basin-averaged warming and its inter-model diversity, aligning with previous studies (Dong & Zhou, 2014; Du & Xie, 2008). This reduced evaporative cooling results from a combination of weaker surface winds and higher near-surface relative humidity (Laîné et al., 2014). The wind reduction is tied to weakened monsoonal circulation during both summer and winter (Parvathi et al., 2017; Sooraj et al., 2015), while the mechanisms driving the relative humidity increase remain poorly understood (Shakespeare & Roderick, 2024). We also find that cloud cover variations also contribute to inter-model diversity through their effect on shortwave radiation, consistent with studies linking global warming uncertainty to cloud feedbacks (e.g., Zelinka et al., 2020). However, our analysis treats shortwave radiation purely as a forcing due to the difficulty of establishing an explicit relationship between cloud cover and SST changes, underscoring the need to better account for cloud feedback effects. These findings highlight that reducing uncertainties in monsoonal wind changes and cloud feedback processes is critical for improving TIO warming projections in CMIP models.

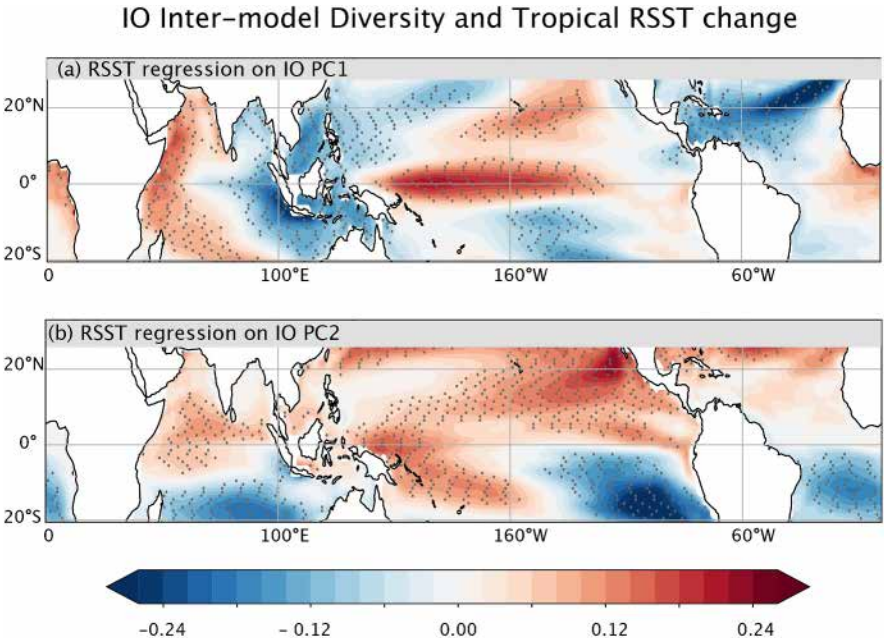

Figure 12. Teleconnections of the two TIO warming patterns with other tropical basins. Map of inter-model regressions of $\Delta T'$ over the entire tropical band to the normalized (a) PC1 and (b) PC2. Stippled regions indicate area where regression values are significantly different from zero at over the 95% confidence level.

One of the two major TIO warming patterns highlighted in this study is the well-documented IOD-like warming (e.g., Zheng et al., 2013). We find that the Bjerknes feedback loop largely determines both its MMM amplitude and inter-model variability, as indicated by the dominant contribution of oceanic processes. While this positive feedback amplifies zonal SST gradient changes, it does not fully explain the initial trigger of its weakening. A stronger negative evaporative feedback over the warmer eastern TIO compared to the cooler western TIO contributes to both the MMM zonal gradient weakening and its inter-model diversity (Figure 9), suggesting it may help to initiate this pattern, consistent with previous studies (e.g., Liu et al., 2015; Zhang & Li, 2014). Additionally, some studies reveal a weakening of the Walker circulation in response to spatially homogeneous warming (Ma et al., 2012; Sharma et al., 2023; Zhang & Li, 2017), which could initiate the zonal SST gradient weakening by altering the equatorial thermocline slope. Others point to the ocean thermostat mechanism (Liu et al., 2015), where seasonal upwelling in the eastern equatorial Indian Ocean during boreal summer and fall moderates warming by bringing up deeper cooler water, consistent with our analyses indicating a reduced warming through oceanic processes in the eastern equatorial Indian Ocean (Figure 8b).

We explore another potential trigger for the weakening of the TIO zonal equatorial SST gradient: interactions with other tropical basins (Cai et al., 2019). Figure 12a highlights that models projecting the strongest IOD-like warming pattern also display an enhanced warming in the western and central Pacific. This Pacific warming may initiate the IOD-like warming pattern by inducing easterly anomalies over the equatorial Indian Ocean, similar to how El Niño events promote positive IOD events at interannual timescales (Cai et al., 2013).

However, this Indo-Pacific connection may be exaggerated in models due to a cold and dry western Pacific bias (Li, Xie, Du, & Luo, 2016), which shifts the atmospheric response westward and may artificially amplify the IOD-like pattern. Additionally, biases specific to the TIO, such as overestimated IOD amplitude (Li, Xie, & Du, 2016) and an unrealistically shallow thermocline in the eastern TIO (G. Wang et al., 2021), further challenge the robustness of this projected pattern. These biases have opposing effects: an overestimated IOD amplitude enhances future IOD-like warming (Li, Xie, & Du, 2016), while an underestimated thermocline slope weakens it (G. Wang et al., 2021). These findings underscore the urgent need to reduce the impact of present-day model biases on TIO warming projections (Lengaigne et al., 2025).

Our results reveal another prominent but less studied warming pattern: the strengthening of the interhemispheric SST gradient. This MMM gradient increase is primarily driven by differential evaporative feedback, where stronger climatological winds in the southern TIO reduce negative latent feedback in that region. Inter-model variability in this pattern is largely linked to differences in cross-equatorial winds changes, which modulate the interhemispheric contrasts in latent heat flux forcing. Specifically, stronger southern TIO winds increase latent heat cooling in the southern hemisphere during boreal summer, while weakened winter monsoon northerlies enhance near-surface humidity in the northern IO, reducing evaporative cooling.

To date, Sharma et al. (2023) is the only study to specifically investigate the mechanisms behind the interhemispheric SST gradient strengthening, focusing on a single CMIP model (Large ensemble simulations of CESM2) projects a *reduced* interhemispheric SST gradient—an outlier among CMIP models. Our heat budget analysis for this model (single member of CESM2; not shown) confirms Sharma et al.'s (2023) interpretation that southern TIO low-cloud cover and shortwave radiation changes drive this weakening. However, it also underscores the model's outlier status, not only due to its atypical interhemispheric SST gradient reduction but also because cloud changes rarely play a dominant role in the 44 other CMIP5/6 models examined. These findings emphasize the importance of broad multi-model analyses to establish robust mechanisms for regional climate change signals.

Figure 12b reveals that the TIO interhemispheric SST gradient change is part of a broader pan-tropical pattern, with similar features in the Pacific and Atlantic Oceans. Our results emphasize the role of enhanced evaporative cooling in driving the MMM cooling in the southern TIO, whereas reduced warming in the southeastern Pacific has been attributed to future increases in wind speed (Xie et al., 2010). Beyond the interhemispheric asymmetry in land distribution (Stouffer et al., 1989), recent studies suggest that enhanced North Atlantic and Pacific warming is linked to the North Atlantic warming hole, which strengthens non-radiative fluxes in the Northern Hemisphere (Park et al., 2024). Given the climatic implications of this asymmetrical oceanic warming pattern, particularly its impact on atmospheric circulation and rainfall (Byrne et al., 2018; Kang et al., 2008; B. Wang et al., 2020), further research is needed to better understand the mechanisms driving interhemispheric SST changes in the tropics and beyond.

While our statistical approach provides valuable insights, it lacks the depth of modeling studies that allows for a more detailed investigation of underlying mechanisms. Future work will use oceanic simulations forced with projected changes in forcing patterns to assess the impact of present-day model biases on TIO SST projections and to better quantify the respective contributions of heat fluxes and wind stress changes.

Appendix A: Indian Ocean Mean and Perturbation Decomposition

The SST change reconstruction equation (Equation 3 in the main text), in its simplified form in terms of forcing (for) and ocean dynamics (O):

$$\Delta T = \frac{\Delta Q_{\text{for}} + \Delta O}{\alpha} \tag{A1}$$

To understand basin-average warming and pattern changes, we further decomposed Equation A1 into mean and perturbation using the Reynolds decomposition formula:

$$\Delta T = \Delta\overline{T} + \Delta T'$$

In which, ΔT represents the total temperature change, an overbar and prime denotes the basin average warming and perturbations from the mean respectively.

Likewise, the above Equation A1 can be written as:

$$\overline{\Delta T} + \Delta T' = \frac{\overline{\Delta Q_{\text{for}}} + \Delta Q_{\text{for}}{}' + \overline{\Delta O} + \Delta O'}{\overline{\alpha} + \alpha'} \tag{A1a}$$

rearranged to:

$$\overline{\Delta T}\,\overline{\alpha} + \Delta T'\overline{\alpha} + \overline{\Delta T}\alpha' + \Delta T'\alpha' = \overline{\Delta Q_{\text{for}}} + \Delta Q_{\text{for}}{}' + \overline{\Delta O} + \Delta O' \tag{A1b}$$

For the basin average warming, we averaged Equation A1b, considering the mean of the mean is mean, and the mean of perturbations is zero. Upon calculation, we find the term $\overline{\Delta T'\alpha'}$ is negligible, and the final equation for basin average warming is:

$$\overline{\Delta T} = \frac{\overline{\Delta Q_{\text{for}}} + \overline{\Delta O}}{\overline{\alpha}} \tag{A2}$$

By subtracting Equation 4 from Equation A1b, we get the equation for the perturbations:

$$\Delta T' = \frac{\Delta Q_{\text{for}}{}' + \Delta O' - \alpha'\overline{\Delta T}}{\alpha} \tag{A3}$$

Where, $\alpha'\overline{\Delta T}$ represents the ocean's flux feedback.

For the final equations, we changed the denominator of Equations A2 and A3 with spatial points average (denoted by overbar) and MMM (denoted by $< >$) of "α", to ensure uniformity in assessing component contributions across models and regions, given the deviation in "α" among models and regions is less than 15% (Figure 2f; and refer methodology). After replacing denominator in Equations A2 and A3 with $\overline{\langle\alpha\rangle}$, the final Equations 4 and 5 are given in the methodology section of the paper.

Appendix B: Model Diversity

To understand the inter-model diversity, we calculated the variance and covariance for total temperature change, mean and perturbation equations. For example, the variance of total temperature change $\Delta\ T$, is the sum of the covariance of each term's contribution with ΔT in Equation 3:

$$\begin{gathered}\Delta\ T = \frac{\Delta Q_{\text{for}}}{\alpha} + \frac{\Delta O}{\alpha}\\ \text{Variance }(\Delta T) = \text{covariance}\left(\frac{\Delta Q_{\text{for}}}{\alpha}, T\right) + \text{covariance}\left(\frac{\Delta O}{\alpha}, T\right)\end{gathered} \tag{B1}$$

Similar calculations are performed for mean and perturbation equations.

Data Availability Statement

The CMIP simulations used in this study is publicly available and can be downloaded from CMIP5 search interface: https://data.ceda.ac.uk/badc/cmip5/ or https://esgf-node.llnl.gov/search/cmip5/ and CMIP6 search interface: https://data.ceda.ac.uk/badc/cmip6/ or https://esgf-node.llnl.gov/projects/cmip6/. All codes developed for conducting analyses, generating results, and creating plots are published in Zenodo (Gopika, 2025).

Acknowledgments
This work is an integral part of the Ph.D. thesis of G.S. registered at the School of Earth, Ocean and Atmospheric Sciences of Goa University, and the CSIR-National Institute of Oceanography (CSIR-NIO). G. S. acknowledges the Council of Scientific and Industrial Research (CSIR), New Delhi for funding her Ph.D. We thank the Director of CSIR-NIO and the Vice Chancellor of Goa University for their support. The authors acknowledge funding from Institut de Recherche pour le Développement (IRD). The authors also acknowledge the World Climate Research Program's Working Group on Coupled Modelling, which is responsible for CMIP, and the climate modeling groups (listed in Table 1) for producing and making their model outputs available. This is NIO contribution 7407.

References

Beal, L. M., Jérôme, V., Mathew, K. R., Li, J. C., Andres, M. S., Annamalai, H., et al. (2020). A road map to IndOOS-2: Better observations of the rapidly warming Indian Ocean. *Bulletin of the American Meteorological Society*, *101*(11), E1891–E1913. https://doi.org/10.1175/bams-d-19-0209.1

Bell, S. S., Chand, S. S., Tory, K. J., Ye, H., & Turville, C. (2020). North Indian Ocean tropical cyclone activity in CMIP5 experiments: Future projections using a model-independent detection and tracking scheme. *International Journal of Climatology*, *40*(15), 6492–6505. https://doi.org/10.1002/joc.6594

Bjerknes, J. (1969). Atmospheric teleconnections from the equatorial Pacific. *Monthly Weather Review*, *97*(3), 163–172. https://doi.org/10.1175/1520-0493(1969)097<0163:atftep>2.3.co;2

Byrne, M. P., Pendergrass, A. G., Rapp, A. D., & Wodzicki, K. R. (2018). Response of the intertropical convergence zone to climate change: Location, width, and strength. *Current Climate Change Reports*, *4*, 355–370. https://doi.org/10.1007/s40641-018-0110-5

Cai, W., Santoso, A., Wang, G., Weller, E., Wu, L., Ashok, K., et al. (2014). Increased frequency of extreme Indian Ocean Dipole events due to greenhouse warming. *Nature*, *510*(7504), 254–258. https://doi.org/10.1038/nature13327

Cai, W., Wu, L., Lengaigne, M., Li, T., McGregor, S., Kug, J. S., et al. (2019). Pantropical climate interactions. *Science*, *363*(6430), eaav4236. https://doi.org/10.1126/science.aav4236

Cai, W., Zheng, X.-T., Weller, E., Collins, M., Cowan, T., Lengaigne, M., et al. (2013). Projected response of the Indian Ocean Dipole to greenhouse warming. *Nature Geoscience*, *6*(12), 999–1007. https://doi.org/10.1038/ngeo2009

Clement, A. C., Seager, R., Cane, M. A., & Zebiak, S. E. (1996). An ocean dynamical thermostat. *Journal of Climate*, *9*(9), 2190–2196. https://doi.org/10.1175/1520-0442(1996)009<2190:aodt>2.0.co;2

Dong, L., & Zhou, T. (2014). The Indian Ocean sea surface temperature warming simulated by CMIP5 models during the twentieth century: Competing forcing roles of GHGs and anthropogenic aerosols. *Journal of Climate*, *27*(9), 3348–3362. https://doi.org/10.1175/jcli-d-13-00396.1

Dong, L., Zhou, T., & Wu, B. (2014). Indian Ocean warming during 1958–2004 simulated by a climate system model and its mechanism. *Climate Dynamics*, *42*(1–2), 203–217. https://doi.org/10.1007/s00382-013-1722-z

Du, Y., & Xie, S.-P. (2008). Role of atmospheric adjustments in the tropical Indian Ocean warming during the 20th century in climate models. *Geophysical Research Letters*, *35*(8), L08712. https://doi.org/10.1029/2008gl033631

Eyring, V., Bony, S., Meehl, G. A., Senior, C. A., Stevens, B., Stouffer, R. J., & Taylor, K. E. (2016). Overview of the Coupled Model Intercomparison Project Phase 6 (CMIP6) experimental design and organization. *Geoscientific Model Development*, *9*(5), 1937–1958. https://doi.org/10.5194/gmd-9-1937-2016

Gopika, S. (2025). Supporting software for Earth's Future 'Drivers of Future Indian Ocean Warming and its Spatial Pattern in CMIP Models Earth's Future. April 10, 2025 Release (Version 1.0) [Software]. *Zenodo*. https://doi.org/10.5281/zenodo.15192169

Gopika, S., Izumo, T., Vialard, J., Lengaigne, M., Suresh, I., & Kumar, M. R. R. (2020). Aliasing of the Indian Ocean externally-forced warming spatial pattern by internal climate variability. *Climate Dynamics*, *54*(1–2), 1093–1111. https://doi.org/10.1007/s00382-019-05049-9

Held, I. M., & Soden, B. J. (2006). Robust responses of the hydrological cycle to global warming. *Journal of Climate*, *19*(21), 5686–5699. https://doi.org/10.1175/jcli3990.1

Hu, S., & Fedorov, A. V. (2019). Indian Ocean warming can strengthen the Atlantic meridional overturning circulation. *Nature Climate Change*, *9*(10), 747–751. https://doi.org/10.1038/s41558-019-0566-x

Izumo, T., Vialard, J., Lengaigne, M., & Suresh, I. (2020). Relevance of relative sea surface temperature for tropical rainfall interannual variability. *Geophysical Research Letters*, *47*(3), e2019GL086182. https://doi.org/10.1029/2019gl086182

Johnson, N. C., & Xie, S.-P. (2010). Changes in the sea surface temperature threshold for tropical convection. *Nature Geoscience*, *3*(12), 842–845. https://doi.org/10.1038/ngeo1008

Kang, S. M., Held, I. M., Frierson, D. M., & Zhao, M. (2008). The response of the ITCZ to extratropical thermal forcing: Idealized slab-ocean experiments with a GCM. *Journal of Climate*, *21*(14), 3521–3532. https://doi.org/10.1175/2007jcli2146.1

Laîné, A., Nakamura, H., Nishii, K., & Miyasaka, T. (2014). A diagnostic study of future evaporation changes projected in CMIP5 climate models. *Climate Dynamics*, *42*(9–10), 2745–2761. https://doi.org/10.1007/s00382-014-2087-7

Lengaigne, M., Pang, S., Silvy, Y., Danielli, V., Gopika, S., Sadhvi, K., et al. (2025). An ocean-only framework for correcting future CMIP oceanic projections from their present-day biases. *ESS Open Archive*.

Li, G., Xie, S.-P., & Du, Y. (2016). A robust but spurious pattern of climate change in model projections over the tropical Indian Ocean. *Journal of Climate*, *29*(15), 5589–5608. https://doi.org/10.1175/jcli-d-15-0565.1

Li, G., Xie, S. P., Du, Y., & Luo, Y. (2016). Effects of excessive equatorial cold tongue bias on the projections of tropical Pacific climate change. Part I: The warming pattern in CMIP5 multi-model ensemble. *Climate Dynamics*, *47*(12), 3817–3831. https://doi.org/10.1007/s00382-016-3043-5

Liu, W., Lu, J., & Xie, S.-P. (2015). Understanding the Indian Ocean response to double CO_2 forcing in a coupled model. *Ocean Dynamics*, *65*(7), 1037–1046. https://doi.org/10.1007/s10236-015-0854-6

Long, S.-M., & Xie, S.-P. (2015). Intermodel variations in projected precipitation change over the North Atlantic: Sea surface temperature effect. *Geophysical Research Letters*, *42*(10), 4158–4165. https://doi.org/10.1002/2015gl063852

Long, S. M., Xie, S. P., & Liu, W. (2016). Uncertainty in tropical rainfall projections: Atmospheric circulation effect and the ocean coupling. *Journal of Climate*, *29*(7), 2671–2687. https://doi.org/10.1175/jcli-d-15-0601.1

Ma, J., & Xie, S. P. (2013). Regional patterns of sea surface temperature change: A source of uncertainty in future projections of precipitation and atmospheric circulation. *Journal of Climate*, *26*(8), 2482–2501. https://doi.org/10.1175/jcli-d-12-00283.1

Ma, J., Xie, S.-P., & Kosaka, Y. (2012). Mechanisms for tropical tropospheric circulation change in response to global warming. *Journal of Climate*, *25*(8), 2979–2994. https://doi.org/10.1175/jcli-d-11-00048.1

Masson-Delmotte, V., Zhai, P., Pirani, A., Connors, S. L., Péan, C., Berger, S., et al. (2021). *Climate change 2021: The physical science basis. Contribution of working group I to the sixth assessment report of the intergovernmental panel on climate change* (Vol. 2, No. 1, p. 2391). Cambridge University Press.

Park, I. H., Yeh, S. W., Dewitte, B., Wang, G., Kirtman, B. P., & An, S. I. (2024). North Atlantic warming hole modulates interhemispheric asymmetry of future temperature and precipitation. *Earth's Future*, *12*(6), e2023EF004146. https://doi.org/10.1029/2023ef004146

Parvathi, V., Suresh, I., Lengaigne, M., Izumo, T., & Vialard, J. (2017). Robust projected weakening of winter monsoon winds over the Arabian Sea under climate change. *Geophysical Research Letters*, *44*(19), 9833–9843. https://doi.org/10.1002/2017gl075098

Pendergrass, A. G., Conley, A., & Vitt, F. M. (2018). Surface and top-of-atmosphere radiative feedback kernels for CESM-CAM5. *Earth System Science Data*, *10*(1), 317–324. https://doi.org/10.5194/essd-10-317-2018

Roxy, M. K., Modi, A., Murtugudde, R., Valsala, V., Panickal, S., Prasanna Kumar, S., et al. (2016). A reduction in marine primary productivity driven by rapid warming over the tropical Indian Ocean. *Geophysical Research Letters*, *43*(2), 826–833. https://doi.org/10.1002/2015gl066979

Saji, N. H., Goswami, B. N., Vinayachandran, P. N., & Yamagata, T. (1999). A dipole mode in the tropical Indian Ocean. *Nature*, *401*(6751), 360–363. https://doi.org/10.1038/43854

Sandeep, S., & Ajayamohan, R. S. (2014). Poleward shift in Indian summer monsoon low level jetstream under global warming. *Climate Dynamics*, *45*(1–2), 337–351. https://doi.org/10.1007/s00382-014-2261-y

Shakespeare, C. J., & Roderick, M. L. (2022). Diagnosing instantaneous forcing and feedbacks of downwelling longwave radiation at the surface: A Simple methodology and its application to CMIP5 models. *Journal of Climate*, *35*(12), 3785–3801. https://doi.org/10.1175/jcli-d-21-0865.1

Shakespeare, C. J., & Roderick, M. L. (2024). What controls near-surface relative humidity over the ocean? *Journal of Advances in Modeling Earth Systems*, *16*(6), e2023MS004168. https://doi.org/10.1029/2023MS004168

Sharma, S., Ha, K.-J., Yamaguchi, R., Rodgers, K. B., Timmermann, A., & Chung, E.-S. (2023). Future Indian Ocean warming patterns. *Nature Communications*, *14*(1), 1789. https://doi.org/10.1038/s41467-023-37435-7

Sooraj, K. P., Terray, P., & Mujumdar, M. (2015). Global warming and the weakening of the Asian summer monsoon circulation: Assessments from the CMIP5 models. *Climate Dynamics*, *45*(1–2), 233–252. https://doi.org/10.1007/s00382-014-2257-7

Stouffer, R. J., Manabe, S., & Bryan, K. (1989). Interhemispheric asymmetry in climate response to a gradual increase of atmospheric CO_2. *Nature*, *342*(6250), 660–662. https://doi.org/10.1038/342660a0

Taylor, K. E., Stouffer, R. J., & Meehl, G. A. (2012). An overview of CMIP5 and the experiment design. *Bulletin of the American Meteorological Society*, *93*(4), 485–498. https://doi.org/10.1175/bams-d-11-00094.1

Vargas Zeppetello, L. R., Donohoe, A., & Battisti, D. S. (2019). Does surface temperature respond to or determine downwelling longwave radiation? *Geophysical Research Letters*, *46*(5), 2781–2789. https://doi.org/10.1029/2019GL082220

Wang, B., Jin, C., & Liu, J. (2020). Understanding future change of global monsoons projected by CMIP6 models. *Journal of Climate*, *33*(15), 6471–6489. https://doi.org/10.1175/jcli-d-19-0993.1

Wang, G., Cai, W., & Santoso, A. (2021). Simulated thermocline tilt over the tropical Indian Ocean and its influence on future sea surface temperature variability. *Geophysical Research Letters*, *48*(6), e2020GL091902. https://doi.org/10.1029/2020gl091902

Xie, S. (2020). Ocean warming pattern effect on global and regional climate change. *AGU Advances*, *1*(1), e2020GL091902. https://doi.org/10.1029/2019av000130

Xie, S.-P., Deser, C., Vecchi, G. A., Ma, J., Teng, H., & Wittenberg, A. T. (2010). Global warming pattern formation: Sea surface temperature and rainfall. *Journal of Climate*, *23*(4), 966–986. https://doi.org/10.1175/2009jcli3329.1

Yim, B. Y., Yeh, S.-W., & Kug, J.-S. (2017). Inter-model diversity of Arctic amplification caused by global warming and its relationship with the Inter-tropical Convergence Zone in CMIP5 climate models. *Climate Dynamics*, *48*(11–12), 3799–3811. https://doi.org/10.1007/s00382-016-3303-4

Ying, J., & Huang, P. (2016a). Cloud–radiation feedback as a leading source of uncertainty in the tropical Pacific SST warming pattern in CMIP5 models. *Journal of Climate*, *29*(10), 3867–3881. https://doi.org/10.1175/jcli-d-15-0796.1

Ying, J., & Huang, P. (2016b). The large-scale ocean dynamical effect on uncertainty in the tropical Pacific SST warming pattern in CMIP5 models. *Journal of Climate*, *29*(22), 8051–8065. https://doi.org/10.1175/jcli-d-16-0318.1

Zelinka, M. D., Myers, T. A., McCoy, D. T., Po-Chedley, S., Caldwell, P. M., Ceppi, P., et al. (2020). Causes of higher climate sensitivity in CMIP6 models. *Geophysical Research Letters*, *47*(1), e2019GL085782. https://doi.org/10.1029/2019gl085782

Zhang, L., & Li, T. (2014). A simple analytical model for understanding the formation of sea surface temperature patterns under global warming. *Journal of Climate*, *27*(22), 8413–8421. https://doi.org/10.1175/jcli-d-14-00346.1

Zhang, L., & Li, T. (2017). Relative roles of differential SST warming, uniform SST warming and land surface warming in determining the Walker circulation changes under global warming. *Climate Dynamics*, *48*(3–4), 987–997. https://doi.org/10.1007/s00382-016-3123-6

Zheng, X. T., Xie, S. P., Du, Y., Liu, L., Huang, G., & Liu, Q. (2013). Indian Ocean dipole response to global warming in the CMIP5 multimodel ensemble. *Journal of Climate*, *26*(16), 6067–6080. https://doi.org/10.1175/jcli-d-12-00638.1